# Stability and dynamics across magnetic phases of vortex-bright type excitations in spinor Bose-Einstein condensates

G. C. Katsimiga,[1,2,3] S. I. Mistakidis,[4,5] K. Mukherjee,[6] P. G. Kevrekidis,[1] and P. Schmelcher[2,3]

[1]*Department of Mathematics and Statistics, University of Massachusetts Amherst, Amherst, Massachusetts 01003, USA*

[2]*Department of Physics, Center for Optical Quantum Technologies, University of Hamburg, Luruper Chaussee 149, 22761 Hamburg, Germany*

[3]*The Hamburg Center for Ultrafast Imaging, University of Hamburg, Luruper Chaussee 149, 22761 Hamburg, Germany*

[4]*ITAMP, Center for Astrophysics, Harvard and Smithsonian, Cambridge, Massachusetts 02138, USA*

[5]*Department of Physics, Harvard University, Cambridge, Massachusetts 02138, USA*

[6]*Department of Physics, Indian Institute of Technology Kharagpur, Kharagpur, West Bengal 721302, India*

(Received 23 March 2022; revised 20 August 2022; accepted 17 November 2022; published 30 January 2023)

The static properties, i.e., existence and stability, as well as the quench-induced dynamics of vortex-bright type excitations in two-dimensional harmonically confined spin-1 Bose-Einstein condensates are investigated. Linearly stable vortex-bright-vortex and bright-vortex-bright solutions arise in both antiferromagnetic and ferromagnetic spinor gases upon quadratic Zeeman energy shift variations. Their deformations across the relevant transitions are exposed and discussed in detail, evincing also that emergent instabilities can lead to pattern formation. Spatial elongations, precessional motion, and spiraling of the nonlinear excitations when exposed to finite temperatures and upon crossing the distinct phase boundaries, via quenching of the quadratic Zeeman coefficient, are unveiled. Spin-mixing processes triggered by the quench lead, among others, to changes in the waveform of the ensuing configurations. Our findings reveal an interplay between pattern formation and spin-mixing processes accessible in contemporary cold atom experiments.

DOI: 10.1103/PhysRevA.107.013313

## I. INTRODUCTION

It is nowadays possible to controllably create Bose-Einstein condensates (BECs) possessing internal degrees of freedom [1–5]. These multicomponent systems, due to the Zeeman splitting of the involved magnetic sublevels, are known as spinor condensates and have been discussed in dedicated reviews [6,7] and books [8–10]. Among spinors with hyperfine spin $F = 1$ or 2, spin-1 BECs represent arguably the most studied class. The two-body interaction of spin-1 bosons features density (or interparticle) and spin interactions. By engineering the internal states using optical and magnetic fields, various magnetic ground states and the related to them first- and second-order phase transitions are now accessible [6]. For instance a $^{23}$Na spinor gas experiences antiferromagnetic (AF) interactions [1,2] whereas $^{87}$Rb [3,4] and $^{7}$Li [5,11] feature weak and strong ferromagnetic (FM) ones.

The spinor ground-state (GS) phase diagram has been exhaustively studied [6]. Alterations due to confinement have been only recently explored within the mean-field [12] and the many-body framework [13]. Additionally, owing to the presence of internal degrees of freedom a plethora of nonlinear excitations bearing a nontopological and a topological character have been proposed theoretically. A partial list of the latter contains (i) one-dimensional magnetic and unmagnetized spinor solitons [14–20], as well as dark-antidark structures [21]; (ii) the realization [22] and the ensuing phase diagram [23] of spinor dark-dark-bright and dark-bright-bright solitary waves, their collisions [24], as well as twisted magnetic solitons [25]; and (iii) spin domains [26,27], monopoles [28–30], quantum knots [31], as well as three- [32] and two-dimensional (2D) skyrmions [33–37], skyrmion and meron textures [38], and nonaxisymmetric vortex patterns [39]. Moreover, half-quantum vortical structures [40–42] can arise from the instability of singular vortices [43], which, in turn, can emerge from the unstable dynamics of nonsingular ones [44]. Filled-core vortices [45], along with the very recently detected singular SO(3) vortex line [46], can also be included in this list. It is also relevant to mention here that the properties of specific vortex structures in homogeneous systems, such as the elliptic one characterized by broken axisymmetry, were recently discussed for the polar (PO) phase in [47,48] and the so-called nematic spin vortices appearing in the easy-plane (EP) PO phase were analyzed in [49]. In the same context, the robustness of confined coreless vortices when the longitudinal magnetization is preserved has been analyzed [50].

Given the enhanced theoretical and experimental [19,20,22,24] recent interest in spinor BECs and the different excitations that can form in their distinct magnetic phases, we hereby consider harmonically trapped quasi-2D, spin-1 BECs featuring either AF or FM spin interactions. Concerning the static properties of the two setups under consideration, we tackle spinorial stationary states that bear at least one vortex component being filled by bright solitons. In comparison to earlier studies [39], a central feature of our work is that

 ©2023 American Physical Society

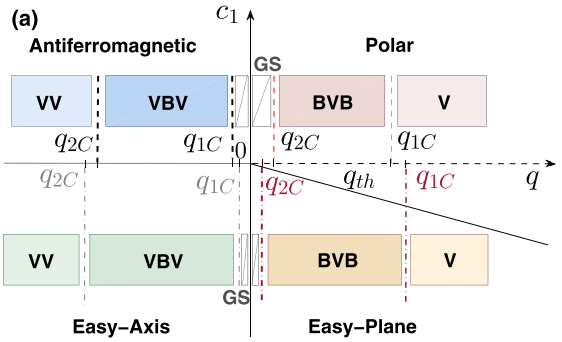


(b)

| AF/FM | *Solut.* | 1C | 2C | 3C |
|---|---|---|---|---|
| $c_1 > 0$ | VBV | $q \geq -0.2$ | $q < -2.5$ | $-2.5 \leq q < -0.2$ |
| | BVB | $q \geq 1.95$ | $q < 0.3$ | $0.3 \leq q < 1.95$ |
| $c_1 < 0$ | VBV | $q \geq -0.14$ | $q < -2.74$ | $-2.74 \leq q < -0.14$ |
| | BVB | $q \geq 2.07$ | $q < 0.15$ | $0.15 \leq q < 2.07$ |

FIG. 1. (a) Schematic illustration of the phase diagram containing the distinct VBV and BVB stationary solutions in the $(c_1, q)$ plane as well as their corresponding deformations under QZ energy shift variations. (b) Intervals of existence of nonlinear excitations of the VB type for AF $c_1 > 0$ (top rows) and FM $c_1 < 0$ (bottom rows) interactions corresponding, respectively, to a spin-1 BEC consisting of $^{23}$Na and $^{87}$Rb atoms. From left to right, each column depicts the occupation of a single (1C), two (2C), and all three (3C) $m_F$ components. A spin component is treated as unpopulated when its occupation, $n_{m_F}$, is less than $1/N$. Here, the total number of particles $N = 10^4$, while the in- and out-of-plane trapping frequencies are $\omega = 2\pi \times 20$ Hz and $\omega_z = 2\pi \times 400$ Hz, respectively. The values of $q$ are given in units of $\hbar\omega$.

we consider vortical states of the same charge and zero net magnetization. Also, a key property of the structures of interest herein is the filling of vortices with bright components when the parameters of the system permit it (see details below). The understanding of the stability properties of such configurations, being addressed herein via a generalized Bogoliubov–de Gennes (BdG) theory [10,51,52], is still far from complete. Only partial results of this kind exist, as, e.g., in the recent study of [49] where the maximal growth rate of the so-called nematic spin vortex state is provided. Here, we build on earlier findings based on simpler one-dimensional settings [23,53], in order to obtain the phase diagram of the identified vortical states, coupled with their corresponding potential instabilities. Triggering the latter can also be valuable, as it is strongly suggested by recent single-component BEC experiments [54], for designing certain topological states in the different spinor phases examining thereafter their dynamical response and spin-mixing processes [54,55]. Our findings indicate that vortex-bright-vortex (VBV) and bright-vortex-bright (BVB) excitations exist as stable configurations for either AF or FM spin-dependent interactions [see Figs. 1(a) and 1(b)]. These excitations experience structural deformations upon quadratic Zeeman (QZ) energy shift variations and importantly they feature narrow QZ intervals where oscillatory instabilities occur [51,56].

Dynamical evolution of perturbed VBV (BVB) entities entails, among others, their irregular (regular) precessional motion, nucleation of cross-shaped spinor patterns, and potential spiraling of the ensuing waveforms. These are findings evincing that spinor BECs provide a fruitful platform for probing instability-related spontaneous pattern formation [57,58]. Further, quench-induced spin-mixing processes are unveiled under QZ energy shift variations at finite temperatures. The inclusion of thermal effects is inspired by their relevance in recent experiments [59,60]. Specifically, population transfer mechanisms are shown to be enhanced for larger values of the QZ coefficient and higher temperatures. Finally, the nonequilibrium dynamics of the vortical spinor configurations reveals the generic activation of their precessional motion, but also deformations where spinors simultaneously exhibit characteristic spatially anisotropic elongations.

The workflow of the present effort is as follows. Section II sets up the model mean-field equations of motion and the linearization method utilized herein. Section III contains our main findings regarding the existence, stability, and dynamics of AF and FM spin-1 BECs. Their quench dynamics at finite temperatures is discussed in Sec. IV. In Sec. V we provide a summary of our results and a list of interesting perspectives for future investigations. In Appendix A, the details of the stability analysis protocol are outlined. Appendix B elaborates on the impact of higher-charge vorticity generalizing earlier instability findings occurring in single-component settings [61], demonstrating also dynamical triangular pattern formation.

## II. EMBEDDING NONLINEAR EXCITATIONS IN THE SPINOR SYSTEM

### A. Mean-field equations

We consider a spin-1 BEC of $N = 10^4$ $^{87}$Rb [22,62] or $^{23}$Na [19] atoms of mass $M$ [63]. A uniform magnetic field $B$ is applied along the transversal $z$ direction, and the system is confined in a quasi-2D harmonic trap. The quasi-2D trap is of the form $V(x, y, z) = M\omega^2(x^2 + y^2)/2 + M\omega_z^2 z^2/2$, obeying the condition $\omega_z \gg \omega$. Here $\omega_z$ denotes the out-of-plane oscillator frequency, i.e., the one along the $z$ direction, and $\omega$ refers to the frequency in the $(x$-$y)$ plane (alias in-plane oscillator frequency). The corresponding three-component wave function, $\Psi(r;t) = (\Psi_1(r;t), \Psi_0(r;t), \Psi_{-1}(r;t))$ with $r \equiv \{x, y, z\}$, represents the distinct spin components, $m_F = \pm 1, 0$, of a spin-1 BEC. Additionally, throughout this work we choose as characteristic length and energy scales the in-plane oscillator length $l_{\rm osc} = \sqrt{\hbar/M\omega}$ and $\hbar\omega$, respectively. Accordingly, space and time coordinates are rescaled as $x' = x/l_{\rm osc}$, $y' = y/l_{\rm osc}$, $z' = z/l_{\rm osc}$, and $t' = \omega t$, respectively, and the wave function is rescaled as $\Psi_{m_F}(x', y', z') = \sqrt{(l_{\rm osc}^3/N)}\Psi_{m_F}(x, y, z)$. However, due to the quasi-2D geometry of the potential considered herein (i.e., $\omega_z \gg \omega$)

the aforementioned three-dimensional wave function can be factorized as follows: $\Psi_{m_F}(x', y', z', t) = \Psi_{m_F}(x', y', t)\phi(z')$. Here, $\phi(z')$ is the normalized GS wave function in the $z$ direction, and $\Psi_{m_F}(x', y', t)$ is the quasi-2D wave function. The latter, with the above choices and rescaling (and dropping the primes for convenience), is described within the mean-field framework by the following dimensionless system of three coupled Gross-Pitaevskii equations (GPEs) [7,18,22]:

$$i\partial_t\Psi_1 = \mathcal{H}\Psi_1 + q\Psi_1 + c_0(|\Psi_{+1}|^2 + |\Psi_0|^2 + |\Psi_{-1}|^2)\Psi_1 + c_1(|\Psi_{+1}|^2 + |\Psi_0|^2 - |\Psi_{-1}|^2)\Psi_1 + c_1\Psi_{-1}^*\Psi_0^2, \tag{1}$$

$$i\partial_t\Psi_0 = \mathcal{H}\Psi_0 + c_0(|\Psi_{+1}|^2 + |\Psi_0|^2 + |\Psi_{-1}|^2)\Psi_0 + c_1(|\Psi_{+1}|^2 + |\Psi_0|^2)\Psi_0 + 2c_1\Psi_1\Psi_0^*\Psi_{-1}, \tag{2}$$

$$i\partial_t\Psi_{-1} = \mathcal{H}\Psi_{-1} + q\Psi_{-1} + c_0(|\Psi_{+1}|^2 + |\Psi_0|^2 + |\Psi_{-1}|^2)\Psi_{-1} + c_1(|\Psi_{-1}|^2 + |\Psi_0|^2 - |\Psi_1|^2)\Psi_{-1} + c_1\Psi_1^*\Psi_0^2. \tag{3}$$

In the above equations, $\mathcal{H} = -\frac{1}{2}(\partial_x^2 + \partial_y^2) + V(x, y)$ is the single-particle Hamiltonian with $V(x, y) = (x^2 + y^2)/2$ denoting the 2D harmonic potential. Moreover, $c_0$ and $c_1$ are the so-called spin-independent and spin-dependent interaction coefficients given by $c_0 = \frac{2N\sqrt{2\pi\kappa}(a_0+2a_2)}{3l_{\rm osc}}$ and $c_1 = \frac{2N\sqrt{2\pi\kappa}(a_2-a_0)}{3l_{\rm osc}}$, respectively, in the units adopted herein. $\kappa = \omega_z/\omega$ is the anisotropy parameter, while the scattering lengths $a_0$ and $a_2$ account for collisions between two atoms belonging to the scattering channels with total spin $F = 0$ and 2, respectively. Additionally, $c_0 > 0$ ($c_0 < 0$) accounts for repulsive (attractive) interatomic interactions, while $c_1 > 0$ and $c_1 < 0$ designate AF and FM spin interactions, respectively. Furthermore, the QZ energy shift, $q$, can be determined via the relation $q = \mu_B^2 B^2/(4\hbar\omega E_{\rm hfs})$, where $\mu_B$ denotes the Bohr magneton and $E_{\rm hfs}$ is the hyperfine splitting. Notably, $q$ can be tuned experimentally by adjusting either the external magnetic field $B$ [64] or the hyperfine splitting $E_{\rm hfs}$ by utilizing a microwave dressing field [65,66].

Moreover, the total number of particles, $1 \equiv \sum_{m_F}\int dx\,dy\,|\Psi_{m_F}(x, y, t)|^2$, is preserved with the population fraction of each spin component being defined as

$$n_{m_F} = \int dx\,dy\,|\Psi_{m_F}|^2, \quad m_F = 0, \pm 1, \tag{4}$$

and satisfying $0 \leqslant n_{m_F} \leqslant 1$. Throughout this work we prescribe that the (similarly conserved quantity of the) net magnetization along the $z$ direction, i.e., $\mathcal{M}_z = \int dx\,dy\,(|\Psi_{+1}|^2 - |\Psi_{-1}|^2)$, remains zero. This, in turn, implies that there is no population imbalance between the symmetric $m_F = \pm 1$ components.

Below, the in-plane trapping frequency is set to $\omega = 2\pi \times 20$ Hz and the transverse one is set to $\omega_z = 2\pi \times 400$ Hz. This leads to an anisotropy parameter $\kappa = 20$ inspired by recent 2D BEC experiments (see, e.g., [57]). Additionally, for AF interactions, a BEC of $^{23}$Na atoms is considered having mass $M = 23$ amu and $s$-wave scattering lengths $a_0 = 2.528\,62$ nm, $a_2 = 2.771\,96$ nm, and therefore $c_0 \approx 0.013N$ and $c_1 \approx 0.000\,39N$ [6,7]. For FM interactions, a BEC of $^{87}$Rb atoms is employed with mass $M = 87$ amu, $a_0 = 5.387$ nm, $a_2 = 5.313$ nm, and thus $c_0 \approx 0.05N$ and $c_1 \approx -0.000\,23N$. The QZ coefficient, $q$, is typically varied within the interval $[-3, 3]$. The latter has been identified to be a representative interval of the principal phenomenology of interest. Unless stated otherwise, the total particle number and the vortex charge are fixed to $N = 10^4$ and $S = 1$, respectively.

### B. Vortex-bright spinor ansatz and BdG approach

Initially (Sec. III), we focus on obtaining stationary solutions of the spinor system of Eqs. (1)–(3) in the form of vortex-bright (VB) solitons [52,67–69] that can occupy all three hyperfine components by utilizing a Newton-Krylov iterative scheme [70]. Specifically, in order to introduce a vortex ($V$) of charge $S$ and a bright ($B$) soliton in the desired $m_F$ component, the following ansatz is applied to the relevant wave functions:

$$\Psi_{m_F}^V(x, y) = \mathcal{H}_m(x)\mathcal{H}_n(y)e^{-(mx^2+ny^2)/2}, \tag{5}$$

$$\Psi_{m_F}^B(x, y) = \exp[-(x^2 + y^2)/2]. \tag{6}$$

In Eq. (5), $\mathcal{H}_m(x) = (-1)^m e^{x^2}\frac{d^m}{dx^m}e^{-x^2}$ and $\mathcal{H}_n(y) = (-1)^n e^{y^2}\frac{d^n}{dy^n}e^{-y^2}$ are the $m$th- and $n$th-order Hermite polynomials, respectively. A singly quantized vortex can be obtained by employing as an initial guess the $(m, n) = (1, 0)$ polynomial, namely, the first excited state for the real part of the relevant wave function, and the $(m, n) = (0, 1)$ for the imaginary part, respectively. In a similar vein, e.g., a doubly quantized vortex ($S = 2$) is realized by a suitable combination of $(m, n)$, i.e., by using $(m, n) = (2, 0) - (0, 2)$ for the real part, and $(m, n) = 2(1, 1)$ for the imaginary one. Subsequently, in Secs. III and IV, the stability properties and the quench-induced dynamics of the previously identified equilibrium states are investigated. Notice that we restrict our investigations to the case where the components contain vortices of the same charge $S$. However, it would be worthwhile to consider in the future also cases in which, e.g., the symmetric spin states include oppositely charged vortices in order to unravel the creation of patterns analogous to the monopoles appearing in three dimensions.

To study the stability of the VBV and BVB configurations found herein, a spectral BdG analysis suitably generalized for 2D spinorial BECs is performed [10,23,51,52]. In delineating the latter, we note that it consists of perturbing the iteratively identified stationary states, $\Psi_{m_F}^0(x, y)$, of each phase via the ansatz

$$\tilde{\Psi}_{m_F}(x, y, t) = \{\Psi_{m_F}^0(x, y) + \epsilon[a_{m_F}(x, y)e^{-i\Omega t} + b_{m_F}^\star(x, y)e^{i\Omega t}]\} \times e^{-i\mu_{m_F}t}. \tag{7}$$

Here, $\epsilon$ is a small amplitude perturbation parameter and $\mu_{m_F}$ with $m_F = 0, \pm 1$ is the chemical potential of each spin component. $\Omega$ and $(a_{m_F}, b_{m_F}^\star)^T$ denote, respectively, the eigenfrequencies and eigenfunctions of the resulting eigenvalue problem that one obtains upon substituting Eqs. (7) into the system of Eqs. (1)–(3) and keeping terms of order $\mathcal{O}(\epsilon)$

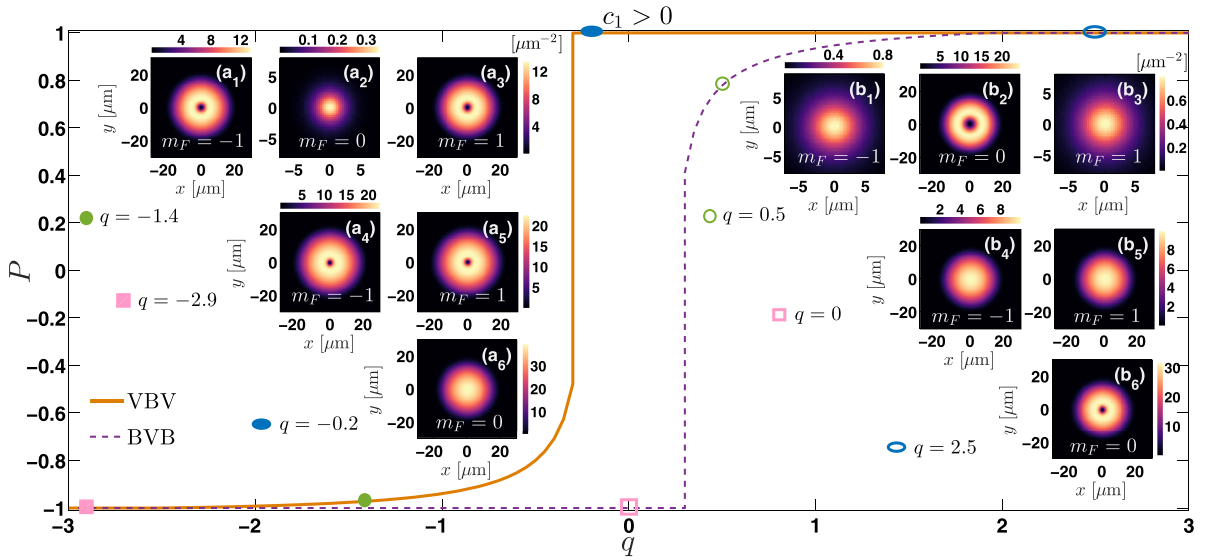


FIG. 2. Polarization, $P$, with respect to the QZ coefficient $q$ for VBV (orange solid line) and BVB (dashed purple line) equilibrium states existing in AF ($c_1 > 0$) spin-1 BECs. Differently colored opaque and transparent markers indicate the value of $q$ for which the distinct solutions are provided. Insets (a1)–(a6) [(b1)–(b6)] illustrate representative density profiles, $|\Psi_{m_F}(x, y)|^2$, of a VBV [BVB] 3C configuration (top row) and its corresponding deformations towards a 2C (middle row) and a 1C (bottom row) stationary state. The components that are not depicted possess zero population. For both types of solutions singly quantized vortices are considered for the relevant in each case $m_F$ component (see legends). The QZ coefficient is expressed in units of $\hbar\omega$.

[10,51,52]. Namely,

$$i\lambda \begin{bmatrix} a_0 \\ b_0 \\ a_1 \\ b_1 \\ a_{-1} \\ b_{-1} \end{bmatrix} = \begin{bmatrix} M_1 & M_2 & M_3 \\ M_4 & M_5 & M_6 \\ M_7 & M_8 & M_9 \end{bmatrix} \begin{bmatrix} a_0 \\ b_0 \\ a_1 \\ b_1 \\ a_{-1} \\ b_{-1} \end{bmatrix}. \tag{8}$$

In the above expression $\lambda \equiv -i\Omega$ and $M_j$ (with $j = 1, \ldots, 9$) are $2\times2$ matrices the explicit form of which is provided in Appendix A. The resulting eigenvalue problem of Eq. (8) is subsequently solved numerically. Note that in 2D spinor condensates BdG analysis of vortical configurations bearing also a bright soliton component is still elusive and only partial results to that effect are available, to the best of our knowledge.

On the dynamical side, in order to study alterations of the stationary states existing in a specific phase when crossing a phase boundary [71], a quench of the QZ energy shift is applied. The quench is performed from an initial (prequench) $q \equiv q_i$ to a final (postquench) value $q \equiv q_f$ in a way that assures penetration to a different phase. To seed population transfer in the quench dynamics, the commutator of the total spin operator with the Hamiltonian has to be nonzero and we achieve this by including weak dissipation into the system. Such dissipation can naturally arise in BEC experiments when a non-negligible thermal gas component is present in the system. Furthermore, in the large particle limit in which we operate it is expected, in line with recent spin-1 BEC experiments [19,20,22,24], that quantum fluctuations are suppressed. For the dynamical evolution of the spinorial system a fourth-order (in time) Runge-Kutta method is used with temporal and spatial discretization $dt = 10^{-4}$ and $dx = dy = 0.05$, respectively, while a (second-order) finite difference scheme is utilized for the spatial derivatives.

## III. STATIC PROPERTIES OF VBV AND BVB SPINOR EXCITATIONS

### A. Antiferromagnetic vortex-bright-type configurations

To tackle the nonlinear excitations of the VB form that arise in the distinct phases of 2D harmonically confined spin-1 BECs, an initial guess provided by Eqs. (5) and (6) is introduced to the time-independent version of the system of Eqs. (1)–(3). Specifically, for AF interactions ($c_1 > 0$), it is well known that two distinct phases exist depending on the value of the QZ energy shift [6,7]. Namely, for $q < 0$ the AF phase is realized while for $q > 0$ the system resides in the PO phase. In the former phase and at the GS level, only the symmetric $m_F = \pm1$ spin components are populated.

Thus, a natural choice for accessing the corresponding excited states is to consider an initial guess where vortices (bright solitons) are embedded in the $m_F = \pm1$ hyperfine states and a bright soliton (vortex) occupies the $m_F = 0$ component. It turns out that among these two, i.e., VBV and BVB, configurations only VBV excitations exist in the AF phase. Representative density profiles are illustrated as insets in Figs. 2(a1)–2(a3). We note in passing that for all vortex entities to be presented throughout we have verified that they are accompanied by the expected $2\pi S$ phase winding (with $S$ denoting the vortex charge). Recall that the polarization, $P = \int dx\, dy\, (|\Psi_0|^2 - |\Psi_1|^2 - |\Psi_{-1}|^2)$, is a measure of population transfer phenomena. It obeys $-1 \leqslant P \leqslant 1$, when all three $m_F$ components (3C) are populated, but $P = 1$ ($P = -1$) if only the $m_F = 0$ ($m_F = \pm1$) state(s) is (are) populated yielding a single (two) component, 1C (2C), configuration. The aforementioned 3C stationary states exhibit polarizations

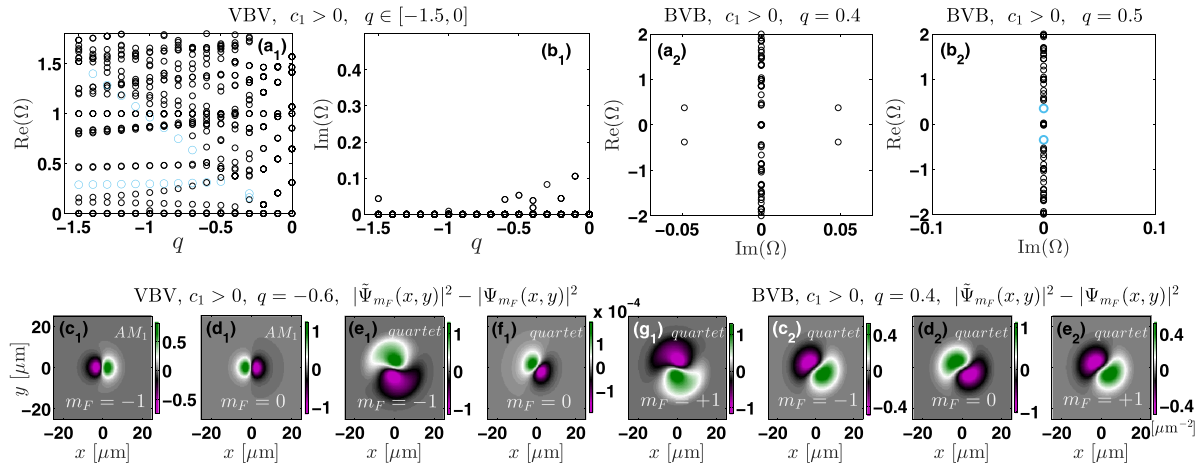


FIG. 3. BdG spectra of 3C (a1, b1) VBV and (a2, b2) BVB stationary states upon a $q$ variation for $c_1 > 0$. In both cases the anomalous modes (AMs) are depicted by light blue circles while the background ones are depicted by black circles. Notice the two AMs present for VBV structures when compared to the single pair occurring for BVB configurations. (c1–g1) [(c2–e2)] 2D contour plots of the difference $\Delta\Psi_{m_F} \equiv |\tilde{\Psi}_{m_F}(x,y)|^2 - |\Psi_{m_F}(x,y)|^2$, demonstrating the effect that the perturbation has on a VBV [BVB] solution for $q = -0.6$ [$q = 0.4$]. The AF BEC consists of $N = 10^4$ sodium atoms confined in a quasi-2D harmonic trap. Note that length and density are given in units of $\mu$m and $\mu\text{m}^{-2}$, respectively; the excitation frequencies $\Omega$ are measured in units of $\omega$ and $q$ in units of $\hbar\omega$.

$-1 < P < 1$ (see orange line in Fig. 2) and their interval of existence is provided in the last column of the table in Fig. 1(b). VBV excitations are further found to deform upon a $q$ variation into highly localized vortices occupying the symmetric spin components as $q$ decreases [Figs. 2(a4)–2(a5)]. These 2C vortices are indeed characterized by $P = -1$ and they exist for all values of $q < -2.5$ that we have checked [see also the fourth column of the table in Fig. 1(b)]. Yet another deformation occurs for the VBV configurations but upon increasing $q$. In this case, each vortex core gradually becomes wider in order to effectively trap [68] the accompanying wider bright soliton of the $m_F = 0$ spin component. This alteration holds until the 1C GS of the PO phase is reached that is, in turn, characterized by $P = 1$ [third column of the table in Fig. 1(b)]. Notice the abrupt jump of $P$ from $P \approx -0.48$, $q = -0.3$ to $P = 1$, $q = -0.2$ (blue opaque ellipse in the $P$ curve of Fig. 2) that signals the abrupt population transfer to the $m_F = 0$ 1C state [Fig. 2(a6)].

Having examined the existence of VBV excitations along with their relevant structural deformations we next explore the stability properties of such configurations. In contrast to earlier predictions mostly focused on energy based considerations [39,47–49] below we utilize a generalized BdG theory to microscopically determine the involved internal modes. As stated earlier, to perform the BdG analysis the ansatz of Eq. (7) is used for this specific stationary solution. The relevant BdG spectra, obtained upon solving the eigenvalue problem of Eq. (8) associated to the VBV solutions, are depicted in Figs. 3(a1)–3(b1). Note that there exist in the spectrum three different pairs of modes lying at the Re($\Omega$) axis around the origin of the Re($\Omega$)-Im($\Omega$) plane, i.e., at Re($\Omega$) = Im($\Omega$) = 0. These zero eigenfrequencies, not visible in the scales shown, are generated by continuous symmetries. The spinor system under study preserves the total particle number (phase invariance of the equations of motion) and the magnetization and further has rotational symmetry, thus explaining the existence of these three pairs. Besides the aforementioned modes, two additional negative-energy ones appear among the remaining modes of the discrete spectra that are denoted by light blue circles. The two distinct trajectories, obtained with respect to $q$, of these so-called anomalous modes (AMs) can be discerned in Fig. 3(a1). These modes are known to correspond to precessional motions of the two vortices within the parabolic trap [67,68]. Additionally, these AMs are quantified through their negative energy or negative Krein signature [51] which for the 2D spinor system reads

$$K = \Omega \int dx\, dy \sum_{(m_F=0,\pm1)} |a_{m_F}|^2 - |b_{m_F}|^2. \tag{9}$$

It should be marked here that the existence of these modes is an immediate byproduct of the fact that the stationary states found herein are excited states of the spinor system. Namely, such modes would be absent in the case of the system's GS. Moreover, as long as these eigenfrequencies maintain their real nature, then their negative Krein signature further indicates that while a stationary solution is dynamically stable, it is simultaneously unstable thermodynamically [10]. The latter, in turn, implies that given a channel of energy dissipation, as in the case of the dissipative spinor system that will be discussed below, these eigendirections will be activated leading to an instability of the ensuing configuration. Notice that upon increasing $q$ so as to reach the phase transition point ($q = 0$), in the vicinity of the latter, the aforementioned negative-energy modes decrease in frequency, with both crossing the zero frequency axis around $q \approx -0.2$. At the same time also a decreasing in the frequency positive-energy mode crosses $\Omega = 0$ and leads to the appearance of the finite imaginary part, Im($\Omega$) $\neq 0$, shown in Fig. 3(b1). The destabilization of the deformed VBV configuration is followed by a change in the Krein signature of the two (previously) negative-energy modes from negative (light blue circles) to positive (black circles).

In addition to the above stability analysis results, there exist narrow intervals of $q$ where oscillatory instabilities [56] take place for the VBV solution. In general, this type of instability stems from collision events involving pairs of positive and negative Krein signature modes resulting in eigenfrequency quartets and also possessing a finite imaginary component $\mathrm{Im}(\Omega) \neq 0$ [23,56]. We must emphasize here that this is yet another key feature related to the theory of AMs, namely, their role in the manifestation of instabilities even at zero temperature. Three such collision events can be readily seen in the BdG spectrum of Fig. 3(a1) appearing, e.g., at $q = -1.5$, $-0.6$, and $-0.4$. The first two are associated with the higher-lying anomalous mode the absence of which for these values of $q$ is transparent while the last one entails the collision and exiting as complex quartets of both negative-energy modes.

Two case examples are considered below for $q = -0.6$, demonstrating the activation of, e.g., the lower-lying anomalous mode ($\mathrm{AM}_1$) along with exploring the oscillatory instability present for this value of $q$. Particularly, Figs. 3(c1)–3(g1) illustrate 2D contours quantifying the density difference between a perturbed and an equilibrium solution $\Delta\Psi_{m_F}(x,y) \equiv |\tilde{\Psi}_{m_F}(x,y)|^2 - |\Psi_{m_F}(x,y)|^2$. The perturbation here consists of adding to the VBV stationary state the eigenvector associated either with $\mathrm{AM}_1$ or with the eigenfrequency quartet identified for $q = -0.6$. Notice the two-lobe structure imprinted in $\Delta\Psi_{m_F}(x,y)$ resembling a $2p$ orbital-like configuration. The lobes are centered around the origin of the ($x$-$y$) plane being parallel to the $y = 0$ axis. They are further found to be asymmetric with respect to $x = 0$ with $\Delta\Psi_{-1}(x > 0, y) > 0$, Fig. 3(c1) [$\Delta\Psi_0(x < 0, y) > 0$, Fig. 3(d1)]. Moreover, the $m_F = +1$ component (not shown) has the same effect with that of $m_F = -1$ when the VBV is perturbed via $\mathrm{AM}_1$ but $\Delta\Psi_{+1}(x,y)$ is complementary to $\Delta\Psi_{-1}(x,y)$ when the VBV is perturbed via the $\mathrm{AM}_2$ mode. However, this is not the case when considering the quartet scenario [Figs. 3(e1)–3(g1)]. The predominant effect of this mode is the asymmetric distribution of $\Delta\Psi_{\pm1}(x,y)$ with respect to $y = 0$ being $\Delta\Psi_{-1}(x, y > 0) > 0$ [$\Delta\Psi_{+1}(x, y < 0) < 0$]. Both components are azimuthally deformed exhibiting a counterclockwise rotation. The $m_F = 0$ one practically remains unaffected, with $\Delta\Psi_0(x,y) \approx 10^{-4}$ featuring an asymmetry along $x = -y$. Finally, it is worth commenting here that the dynamical evolution of the excited, with $\mathrm{AM}_1$, VBV entity leads to its precessional motion where the entire VBV rotates around the trap, whereas exciting the configuration with $\mathrm{AM}_2$ results in a rotating cross-shaped pattern in which the vortex components perform an antiphase oscillation around each other and the $m_F = 0$ bright component remains unaltered. This antiphase vibration leads, in turn, to an overall breathing of the BEC background.

For AF interactions but for $q > 0$, namely, within the PO phase, the preferable configuration consists of a solely occupied $m_F = 0$ spin component. Since this component, according to the GS of the system [7], is expected to become the majority one, in our search for nonlinear excitations arising in this phase we choose to imprint a vortex on it. Consequently, bright solitons are plugged in the remaining $m_F = \pm 1$ spin components. With such an initial guess, indeed, BVB stationary solutions are captured for $0.3 \leqslant q < 1.95$ [see also the relevant fifth column of the table in Fig. 1(b)]. Characteristic density contours of such a BVB structure are presented as insets in Figs. 2(b1)–2(b3). Notice that similarly to the VBV configurations, the BVB stationary states are characterized by $-1 < P < 1$ (see the purple line in Fig. 2) and they also experience two deformations with respect to $q$. One deformation is rather gradual as captured by the slope of the polarization as $q$ increases, leading to a single highly localized vortex occupying the $m_F = 0$ hyperfine state [see Fig. 2(b6) and the relevant third column of the table in Fig. 1(b)]. In contrast, as $q$ decreases towards the first-order transition boundary ($q = 0$) separating the PO and the AF phase, an abrupt deformation of the BVB configuration to the 2C state, reminiscent of the GS of the AF phase, occurs [see Figs. 2(b4) and 2(b5) and the fourth column of the table in Fig. 1(b)] around $q = 0.3$. Notice that both the VBV and the BVB configurations feature smooth deformations towards the 2C and the 1C vortex state, respectively. In the opposite $q$ direction a sharp transition takes place when the relevant phase boundary is approached to 1C and 2C zero vortex states, respectively. This behavior of the polarization is in direct contrast to the corresponding sharp transition occurring on the GS level, i.e., in the absence of nonlinear excitations (results not shown here for brevity) [6,7].

BVB excitations turn out to be linearly stable configurations for all values of $q \in (0.4, 1.95)$, with a relevant example shown in the BdG spectrum of Fig. 3(b2), e.g., for $q = 0.5$. Due to the single vortex contained in this configuration, only a single pair of negative-energy modes is present in this spectrum. According to our discussion above, when activated, i.e., upon adding the associated to it eigenvector to the BVB solution, this mode leads to the precessional motion of the BVB structure. It is only for significantly deformed BVB configurations, namely, for states where the bright soliton dominates the configuration corresponding to $q \leqslant 0.4$, that oscillatory instabilities [like the one depicted in Fig. 3(a2)] appear. In order to appreciate the effect of the emergent eigenfrequency quartet on the BVB solution, we have added to the latter the corresponding quartet eigenvector. A close inspection of the associated density difference $\Delta\Psi_{m_F}(x,y)$ illustrated in Figs. 3(c2)–3(e2), reveals that such an addition leads to an asymmetric across the antidiagonal ($x = -y$) BVB structure having $\Delta\Psi_{\pm1}(x > 0, y) > 0$ and $\Delta\Psi_0(x > 0, y) < 0$. In all cases a counterclockwise rotation takes place that is in turn related to the precessional motion of the entire BVB entity observed in the dynamics. Finally, the anomalous mode ceases to exist for $q < 0.3$ signaling the transition to the GS of the AF phase. Moreover, we emphasize at this point that the robustness of stable VBV and BVB stationary states has been also dynamically confirmed by monitoring their spatiotemporal evolution for times up to $t = 2.0$s.

### B. Ferromagnetic VBV and BVB spinors

Turning to FM spin interactions ($c_1 < 0$) three phases can be realized as $q$ is varied, supporting GSs with an occupancy ranging from 1C to 3C [6]. In particular, the so-called 1C fully magnetized along the $+z$ ($-z$)-direction easy-axis (EA) phase exists for $q < 0$. Since we operate in the regime where the harmonic oscillator length is smaller than the spin-healing length, phase separation is absent in our setting. The case

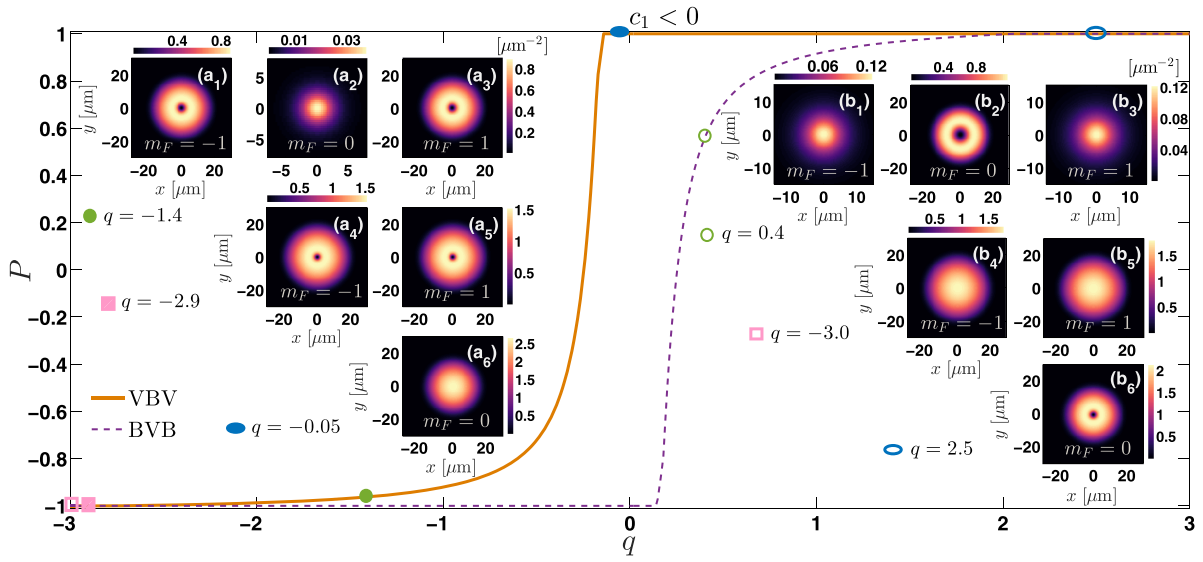


FIG. 4. Polarization, $P$, as a function of the QZ coefficient $q$ for the BVB and VBV equilibrium states occurring in the distinct phases of a spin-1 FM ($c_1 < 0$) condensate. Insets on the left-hand [right-hand] side of (a1)–(a6) [(b1)–(b6)] showcase representative examples of the $m_F$ densities, $|\Psi_{m_F}(x, y)|^2$, of a 3C VBV [BVB] configuration together with its relevant 1C and 2C deformed structures (see legends), as $q$ is varied. The corresponding QZ values in each of the aforementioned cases are also indicated for the individual stationary solutions, with opaque and transparent markers in the polarization curves pointing explicitly at each specific value. Our results are presented in dimensional units, i.e., length is measured in $\mu$m, density in $\mu m^{-2}$, and $q$ in $\hbar\omega$.

where the relevant inequality is reversed, while interesting in its own right, is outside the scope of the present work and hence deferred to future studies. The 3C EP phase occurs for $0 < q < q_T$ and the 1C PO phase is characterized by $q \geqslant q_T$ [6,12,23]. In the latter two inequalities $q_T = 2c_1 n$ (which equals 0.05, for our chosen parameters) designates the threshold between the involved phases with $n$ being the peak density at the trap center. In this FM spinor setting, VBV stationary states are identified for $-2.74 \leqslant q < -0.14$ [fifth column of the table in Fig. 1(b)]. These states possess zero net magnetization and $-1 < P < 1$ as shown in Fig. 4. They also have density profiles, $|\Psi_{m_F}(x, y)|^2$, similar to their AF siblings [Figs. 4(a1)–4(a3)]. Strikingly, FM VBV waves are more persistent configurations when compared to their AF counterparts. They are seen to penetrate deeper into the EA phase before deforming into a 2C vortex [Figs. 4(a4) and 4(a5)] structure for smaller $q$ values [fourth column of the table in Fig. 1(b)]. They further transform slower to the PO GS [Fig. 4(a6)] following an increment of $q$ towards the phase transition boundary ($q = 0$). As such the corresponding polarization curve is found to be right-shifted, thus being closer to the origin when compared to the relevant AF one.

For $0 < q < q_T$, i.e., within the EP phase, the existence of BVB stationary states is also unveiled and presented in Fig. 4. It is noteworthy that FM BVB structures also feature larger $q$ intervals of existence in comparison to their AF analogs [fifth column of the table in Fig. 1(b)]. These structures penetrate the PO regime with the underlying 3C densities as depicted in the insets of Figs. 4(b1)–4(b3). Recall that at the GS level the PO phase exists for $q \geqslant q_T$. Eventually, the 3C BVB structure deforms into the 1C vortex configuration illustrated, e.g., for $q = 2.5$ in Fig. 4(b6). The existence of these states is (parametrically) prolonged also following a decrease of $q$ until a 2C Thomas-Fermi state is reached within the EA phase [Figs. 4(b4) and 4(b5)]. This has as a result a left-shifted polarization curve that is closer to the origin when compared to the relevant AF one.

Investigating the stability of both configurations we find that, as their AF counterparts, VBV and BVB stationary states experience stable intervals of existence. This result can be verified by inspecting the BdG spectra shown in Fig. 5(a1) for the VBV solution and in Figs. 5(a2) and 5(b2) for the BVB one. Notice that in both cases and for the parametric intervals shown, all eigenfrequencies maintain their real nature, i.e., $\mathrm{Im}(\Omega) = 0$. However, these structures further feature narrow $q$ intervals where oscillatory instabilities occur. One such example is presented regarding the VBV entity for $q = -1.2$ in the BdG spectrum of Fig. 5(b1). Similarly to the AF cases discussed above, also here the emergence of an eigenfrequency quartet is observed, that owes its presence to the collision of the higher-lying negative-energy mode, $\mathrm{AM}_3$, with a positive-energy one. Importantly though, and also in sharp contrast to the AF VBV solutions, three instead of two AMs appear in the spectrum of this configuration. As stated earlier, since two vortices participate in this configuration two anomalous mode pairs are to be expected for this stationary state. Thus, we initially investigate further the presence of the lowest-lying mode, namely, $\mathrm{AM}_1$. This mode appears remarkably close to the zero eigenfrequency axis and remains near the latter as $q$ is varied till its destabilization slightly below the threshold separating the EA and the EP, i.e., at $q = -0.2$. $\Delta\Psi_{\pm1}(x, y)$ has a four-lobe spatial distribution closely resembling a $3d_{xy}$ orbital configuration which is further found to be slightly rotated counterclockwise with respect to the $x = 0$ axis. A similar outcome is evidenced for $S = 2$ VBV solutions as discussed in Appendix B and visualized, e.g., in Fig. 10(h1). On the other hand, $\mathrm{AM}_1$ has a vanishing impact on the relevant bright component, with $\Delta\Psi_0(x, y) \approx 10^{-8}$. Particularly, $\mathrm{AM}_1$

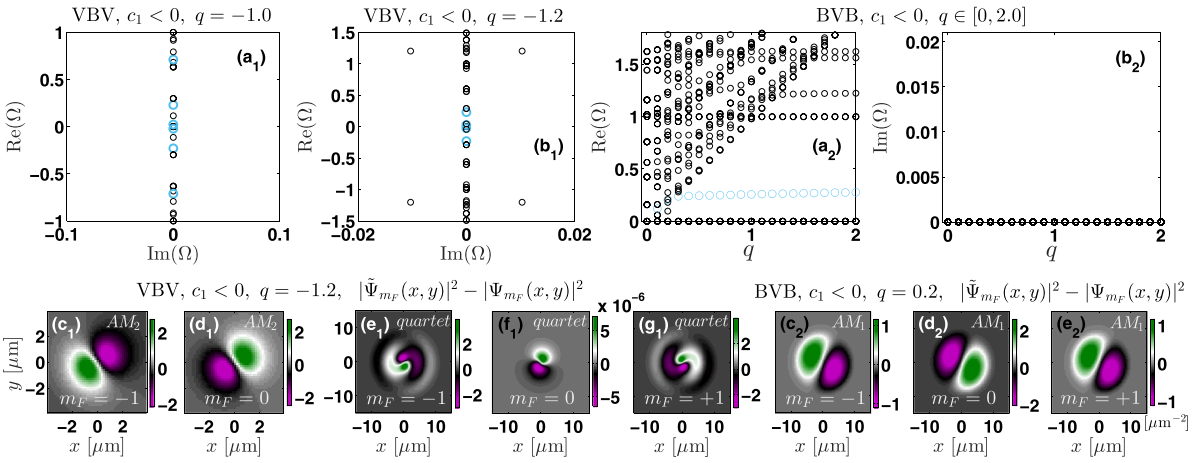


FIG. 5. Same as Fig. 3 but for $c_1 < 0$. Light blue circles denote the AMs present in the spectra and black circles are used for the background modes. Contrary to AF interactions, FM VBV entities feature three anomalous mode pairs but a single pair is present for BVB configurations. (c1–g1) [(c2–e2)] $\Delta\Psi_{m_F} \equiv |\tilde{\Psi}_{m_F}(x,y)|^2 - |\Psi_{m_F}(x,y)|^2$ quantifies the difference between a perturbed and an equilibrium VBV [BVB] solution for $q = -1.2$ [$q = 0.2$]. The FM BEC consists of $N = 10^4$ rubidium atoms confined in a quasi-2D harmonic trap, while length, density, $\Omega$, and $q$ are given in units of $\mu$m, $\mu\mathrm{m}^{-2}$, $\omega$, and $\hbar\omega$.

leads dynamically to an anisotropic spatial elongation of the two vortices that perform a precessional type of motion but with the vortices in the $m_F = \pm 1$ components rotating with a $\pi$ phase difference around each other and a bright soliton that remains set throughout the evolution. As such, this is a mode involving intercomponent dynamics, rather than the intracomponent ones, associated with the vorticity of the VBV structure.

Next, we appreciate the effect that the remaining two AMs have VBV solutions while we note that their destabilization takes place at $q = -0.05$. Considering the eigenvector related to $\mathrm{AM}_2$ results in an asymmetric $2p$ orbital-like distribution of $\Delta\Psi_{m_F}(x,y)$, with the two lobes oriented along the antidiagonal $x = -y$ as showcased in Figs. 5(c1) and 5(d1). It also holds that $\Delta\Psi_{-1}(x > 0, y) < 0$ and $\Delta\Psi_0(x > 0, y) > 0$. Note that a similar $2p$ orbital configuration is also obtained for FM $S = 2$ VBV spinors (see the relevant discussion around $\mathrm{AM}_3$ and $\mathrm{AM}_4$ in Appendix B). This mode leads upon activation to the normal or regular precession of the VBV structure. Namely, the two vortices are on the same side and oscillate around the trap center with the bright soliton following their motion. A much more drastic deformation is evidenced when the solution is perturbed through the eigenvector of $\mathrm{AM}_3$ leading to an asymmetric azimuthally rotated $\Delta\Psi_{m_F}(x,y)$ for the symmetric $m_F = \pm 1$ vortex components analogous to the one found for AF VBV equilibrium states [see Figs. 3(e1) and 3(g1)]. Also here, $\Delta\Psi_0(x,y) \approx 10^{-6}$ has a vanishing effect for the bright soliton component. As we shall show in the dynamics below, once excited, the mode $\mathrm{AM}_3$ leads to a different form of precession of the VBV solution. Here, the precession of the VBV consists of two vortices hosted in the $m_F = \pm 1$ being antidiametrically located with respect to the center and performing oscillations that have a $\pi$ phase difference with respect to one another, while the $m_F = 0$ bright soliton component remains intact. However, this motion becomes responsible for an instability when $\mathrm{AM}_3$ collides with a positive Krein background mode. Recall that whenever such a collision takes place an eigenfrequency quartet occurs in the BdG spectrum instead of the ensuing AM pair. Indeed, notice that, e.g., $\mathrm{AM}_3$ is absent in Fig. 5(b1) giving rise to the observed quartet. In this latter case as it is shown in Figs. 5(e1)–5(g1), a spiral is imprinted in the density difference $\Delta\Psi_{\pm 1}(x,y)$ being of a complementing nature among these two hyperfine components, yet minuscule for the $m_F = 0$ one [Fig. 5(f1)]. This leads in turn dynamically to a spiraling of the 2D VBV entity, an outcome caused by the oscillatory instability.

As an example for the BVB solution, we choose the one of a significantly deformed, i.e., close to threshold, BVB excitation [Figs. 5(c2)–5(e2)]. It turns out that the bright soliton hosted in the $m_F = \pm 1$ spin components dominates the configuration for $q = 0.2$. This bright dominated entity is additionally found to be significantly broadened. Its width becomes comparable to the size of the background cloud, suggesting that the BVB character of this solution is lost. Perturbing this state with the eigenvector associated with the single—in this case—AM pair leads to a two-lobe asymmetric density difference resembling a $2p$ orbital for all three hyperfine states. The two lobes are oriented along the diagonal but experience an asymmetry, with $\Delta\Psi_{\pm 1}(x,y) < 0$ for $x = -y$ and $\Delta\Psi_0(x,y) > 0$, along the antidiagonal. Featuring in this way a similar yet inverted behavior to the one found for FM VBV but also to FM $S = 2$ BVB spinors (Appendix B). Snapshots during the spatiotemporal evolution of this perturbed entity are provided in Figs. 6(a1)–6(c5). As expected, the precessional motion of the entire BVB structure is observed from the initial stages of the dynamics, with the bright soliton $m_F = \pm 1$ components remaining trapped in the course of the evolution around the vortex core [see Figs. 6(a1)–6(c5)]. For comparison, in the bottom panels of Figs. 6(d1)–6(f5), a perturbed VBV excitation via the eigenvector of $\mathrm{AM}_3$ is presented for $q = -1.0$. Two key findings are worth commenting on here. The one concerns the fact that even though the amplitude of the perturbation for both structures is the same, the precession of the VBV excitation is not as pronounced as the one observed for the deformed

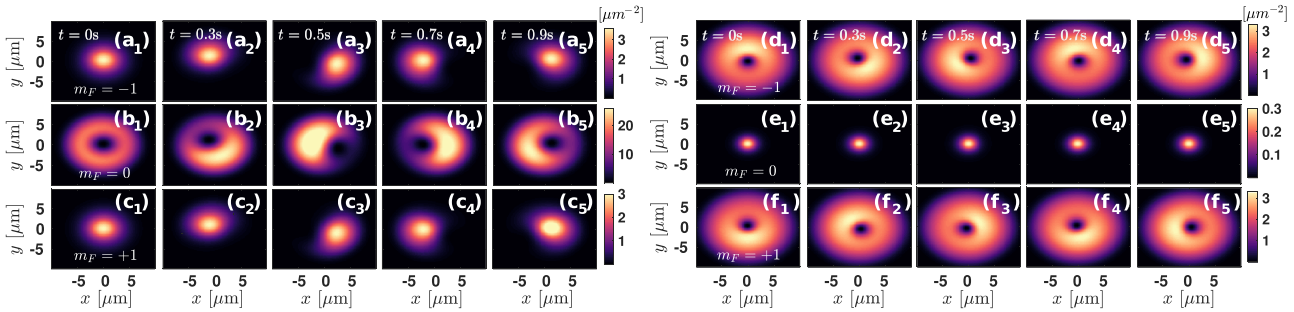


FIG. 6. (a1–c5) [(d1–f5)] Snapshots of the $m_F$-component density, $|\tilde{\Psi}_{m_F}(x, y)|^2$, of a perturbed FM BVB [VBV] solution for $q = 0.2$ [$q = -1.0$]. The distinct spin components are illustrated, respectively, from top to bottom (see the legends) while each column corresponds to a fixed time instant ranging from $t = 0$s to 0.9s. For both the BVB and the VBV structure the prevailing feature is their regular and irregular precessional motion, being activated upon adding the eigenvector associated with the single and the $AM_3$ negative-energy mode, respectively (see the text). All quantities shown are given in dimensionful units.

BVB solution. However, and even more importantly, irregular precession is featured by the VBV structure with the two vortices being out of phase throughout their motion. This is an outcome that has a drastic effect also on the bright soliton which, contrary to the BVB state, now remains unaffected.

Finally, in order to emulate the presence of a finite thermal fraction being usually present in cold atom experiments we introduced the ansatz $\Psi^{\rm pert}_{m_F} = \Psi^0_{m_F}(x, y)[1 + \varepsilon\delta(x, y)]$ to the $m_F$ component wave function [72]. In this expression, $\epsilon$ accounts for the thermal fraction and $\delta(x, y)$ denotes a normally distributed perturbation with zero mean and variance unity [57]. Generically, this ansatz allows for the activation of the respective AM in the course of the evolution. Additionally, it should be noted that the AMs are converted to unstable eigendirections in the presence of a thermal fraction, correspondingly dominating the BEC dynamics, similarly to what is known, e.g., for two-component condensates [73]. This way, the destabilization mechanisms found above would be evident in a corresponding experimental realization.

## IV. QUENCH DYNAMICS ACROSS MAGNETIC PHASES

Having explicated the static properties of VBV and BVB nonlinear excitations, in the following we aim at addressing alterations of the ensuing waveforms being subjected to quenches of the $q$ parameter in order to cross the distinct magnetic phase boundaries (see also Figs. 2 and 4). To monitor the quench-induced dynamical evolution of the spinor gases at hand in an experimentally relevant fashion [5], we expose them to finite temperatures. Note that quenches are routinely utilized in spin-1 ultracold atom experiments to probe transition boundaries [59], spin turbulence, and the related to it half-quantum vortex generation [60] but also to study matter-wave jet formation [11]. Contrary to the above, here we use quenches at finite temperatures (i) to activate the internal motion of the identified vortical spinors, (ii) to facilitate population transfer among the components, and (iii) to study structural deformations of both BVB and VBV configurations across the distinct magnetic phases. In the mean-field framework in order to qualitatively account for thermal effects we utilize the following coupled system of three dissipative GPEs [23,72]:

$$(i - \gamma)\partial_t \Psi_0 = \tilde{\mathcal{H}}\Psi_0 + c_0(|\Psi_{+1}|^2 + |\Psi_0|^2 + |\Psi_{-1}|^2)\Psi_0 + c_1(|\Psi_{+1}|^2 + |\Psi_0|^2)\Psi_0 + 2c_1\Psi_1\Psi_0^*\Psi_{-1}, \tag{10}$$

$$(i - \gamma)\partial_t \Psi_{\pm 1} = \tilde{\mathcal{H}}\Psi_{\pm 1} + c_0(|\Psi_{+1}|^2 + |\Psi_0|^2 + |\Psi_{-1}|^2)\Psi_{\pm 1} + c_1(|\Psi_{\pm 1}|^2 + |\Psi_0|^2 - |\Psi_{\mp 1}|^2)\Psi_{\pm 1} + q\Psi_{\pm 1} + c_1\Psi_{\mp 1}^*\Psi_0^2. \tag{11}$$

In Eqs. (10) and (11) $\tilde{\mathcal{H}} \equiv \mathcal{H} - \mu_{m_F}$ and $\gamma \ll 1$ is a dimensionless dissipative parameter that is connected to the spinor systems' temperature [74]. Typically, $\gamma \in [2\times10^{-4}, 2\times10^{-3}]$ refers to temperatures $T \in [10, 100]$ nK as has been discussed, e.g., in [74].

Representative examples among the extensive investigations performed herein are presented in Figs. 7(a1)–7(c4) and 7(d1)–7(f4) regarding the density evolution for AF and FM spin interactions, respectively, with $\gamma = 0.0023$. In the former case, we monitor the dynamics of an AF BVB excitation once quenched from the PO phase having $q_i = 0.3$ towards the AF phase with postquench QZ coefficient $q_f = -1.0$. It becomes apparent that population transfer from $m_F = 0$ to $\pm 1$ states takes place [see also Fig. 8(b1)] from the initial stages of the quench-induced dynamics triggering the precession of an initially stationary spinorial BVB structure. This motion is accompanied by a prominent elongation along with the instantaneous rotation of all three spin constituents. Moreover, the vortex experiences a structural deformation reminiscent of a doughnutlike pattern: an outcome that is further captured by the two mode motion of the relevant temporal evolution of the populations of the individual components illustrated in Fig. 8(b1). This two mode motion is characterized by rapid oscillations of the populations and a long-time transfer (not shown in the presented timescales) where exchange of the populations between $m_F = 0$ and $\pm 1$ takes place. Notice that the bright soliton $m_F = \pm 1$ components remain trapped around the vortex core, following its composite motion throughout the evolution. Turning to FM interactions and upon considering a quench from $q_i = 0.15$ (EP phase) to $q_f = 4.5$ (PO phase) it is observed that the precessional

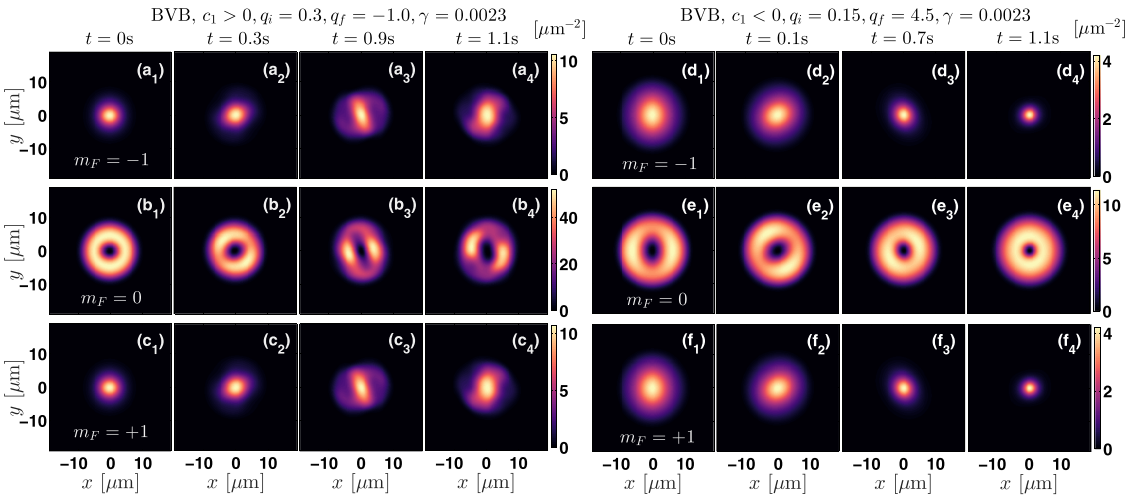


FIG. 7. Instantaneous density profiles of a BVB solution illustrating the $m_F = -1$ (top), $m_F = 0$ (middle), and $m_F = +1$ (bottom) components, upon considering quenches that (a1–c4) either cross the phase boundary separating the PO and the AF phase of an AF spin-1 BEC or (d1–f4) enter deeper in the PO regime for a FM spinor gas, respectively (see legends). For AF interactions, the structural deformation of the BVB entity corresponding to a precession and simultaneous spatial elongation of all components is monitored for times up to $t = 1.1$s. The vortical pattern at $m_F = 0$ acquires a dipolar spatial form. In contrast, the precessional motion of the BVB configuration along with a simultaneous population transfer from the $m_F = \pm 1$ states to the $m_F = 0$ component dominates the evolution for FM interactions. In both cases the damping parameter is $\gamma = 0.0023$ while each system contains $N = 10^4$ atoms. Note that time, length, and density are measured in units of s, $\mu$m, and $\mu\text{m}^{-2}$, respectively, while QZ is measured in $\hbar\omega$.

motion constitutes the dominant dynamical mode, entailing an arguably faster spin-mixing process when compared to the aforementioned AF scenario.

In order to shed light onto the underlying spin-mixing processes triggered by the quench, a close inspection of the temporal evolution of the population of the individual components, $n_{m_F}(t)$, is performed. Specifically, Figs. 8(a1)–8(c2) and 8(d1)–8(f2) capture the essence of our findings for a wide selection of pre- and postquench QZ energies and for distinct $\gamma$ values. AF ($c_1 > 0$) and FM ($c_1 < 0$) condensates are treated on equal footing. For both spinor settings, transitions across the distinct magnetic phases are initiated from the relevant in each phase 3C VBV and BVB stationary states towards the corresponding 2C or 1C configuration.

Particularly, our key observations are the following. Irrespectively of the spinorial BEC system, spin-mixing processes are activated from the initial stages of the quench-induced dynamics. We find that population transfer occurs faster for larger postquench values $q_f$ accessing this way states that are deeper in the relevant magnetic phase [Figs. 8(a1), 8(b2), 8(d1), and 8(e2)]. However, it is found to be more suppressed for VBV excitations as compared to BVB ones. This suppression occurs also for both types of entities when the relevant transition entails quenches within the same phase when compared to transitions that cross distinct phase boundaries. Additionally, spin mixing is accelerated for a larger dissipation parameter $\gamma$ being in turn related to higher temperatures [see for instance Figs. 8(c1), 8(c2), 8(f1), and 8(f2)]. We also remark that slightly enhanced intercomponent population transfer arises for AF rather than FM interactions as can be inferred by comparing Figs. 8(a1) and 8(d2) due to the larger spin-spin interaction in the former case. Finally, it is important to note here that the aforementioned findings occur during the nonequilibrium dynamics of higher charge excitations. However, in this case, the spin-mixing processes discussed above are found to be relatively accelerated.

## V. CONCLUSIONS AND FUTURE PERSPECTIVES

In the present work the existence, stability, as well as quench-induced dynamics of VB-type nonlinear excitations arising in 2D harmonically trapped spin-1 antiferromagnetic and ferromagnetic BECs have been explored. Our investigation has been focusing on variations of the quadratic Zeeman energy shift so as to access and subsequently cross the distinct magnetic phases of such settings. A systematic Bogoliubov–de Gennes linearization analysis has been utilized for the extraction of the stability properties of the considered nonlinear excitations.

In particular, the existence of VBV and BVB stationary states has been exemplified, with the former being present in the antiferromagnetic and the easy-plane phases for antiferromagnetic and ferromagnetic spin interactions, respectively. In contrast, BVB solutions appear in the polar phase of either antiferromagnetic or ferromagnetic spinors. In this latter scenario, stable BVB structures are also found within the easy-plane phase. In both settings deformations of the ensuing waveforms as the associated transition boundary is approached are explicated complementing this way the phase diagram of this type of nonlinear excitations in the $(c_1, q)$ plane.

It turns out that, independently of their flavor and also of their charge, the aforementioned entities exhibit stable intervals of existence that can be interrupted by narrow windows where oscillatory instabilities take place. Indeed, we have elaborated on the number of anomalous mode eigendirections that the structures bear and thus the number of potential instabilities, as well as illustrated when these instabilities

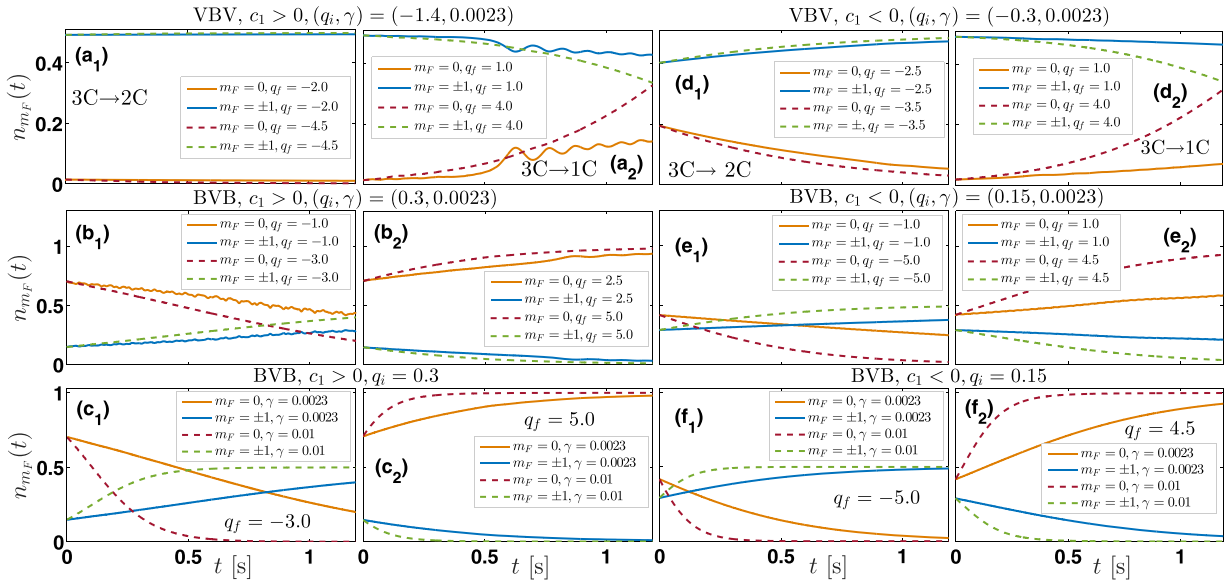


FIG. 8. (aj–cj) [(dj–fj)] With $j = 1, 2$, temporal evolution of the populations, $n_{m_F}(t)$, of the different spin components considering quenches of the QZ coefficient at finite temperatures both within the same magnetic phase and upon crossing distinct phases of an AF [FM] spinor gas (see legends). Spin mixing is triggered in all cases being more suppressed for VBV excitations as compared to the BVB ones and for both types of entities when the relevant transition entails quenches within the same phase. In all cases, the initial-state configuration, having a prequench value $q \equiv q_i$, refers to the underlying in each phase 3C stationary state transitioning either from 3C → 2C or from 3C → 1C states being characterized by different postquench QZ coefficients $q \equiv q_f$ (see legends). All quenches are considered for fixed $\gamma$ that is either $\gamma = 0.0023$ or $\gamma = 0.01$ (see legends). The AF [FM] condensate $c_1 > 0$ [$c_1 < 0$] consists of $N = 10^4$ $^{23}$Na [$^{87}$Rb] atoms. Note also that time is provided in dimensional units being of the order of few seconds and $q$ is given in units of $\hbar\omega$.

may materialize as a result of collision of these anomalous modes with positive-energy ones. We have also monitored the dynamical outcome of excitation of the different anomalous modes. The robustness or unstable dynamics of the above-described entities is confirmed accordingly, demonstrating for instance the precessional motion of VBV and BVB spinors and their structural deformation towards—among others—triangular-shaped patterns.

We have further investigated the quench-induced dynamical evolution of the aforementioned three-component spinors at finite temperatures so as to appreciate the system's dynamical response. Here, it is found that spin-mixing processes occur faster for larger postquench quadratic Zeeman energy shifts and an increasing dissipation parameter. Also, population transfer is slightly enhanced when considering antiferromagnetic instead of ferromagnetic spin-dependent interactions. Monitoring the nonequilibrium dynamics reveals, among others, the activation of the precessional motion along with a spatial elongation of the spinorial nonlinear excitations, irrespectively of their specific nature and spin interactions. The above processes are accelerated when higher charge vortices are contained in the spinorial configuration. The latter also bear a significantly larger number of anomalous modes and, thus, potentially unstable eigendirections.

There exist several extensions of the present work worth pursuing in future endeavors. A straightforward generalization would be to study the quench dynamics in a $^7$Li spin-1 BEC where the strong ferromagnetic spin interaction would certainly enhance the spin-mixing processes which might be possibly associated with a richer pattern formation. A detailed investigation of, e.g., $S = 3$ vortical spinors, that we barely touched upon herein, in symmetry broken settings would facilitate the engineering of exotic pattern formation with atomic orbital-like signatures. Additionally, exploring the interaction effects of vortex lattices as well as their stability and dynamics in spinor setups is of direct relevance, due to the potential of inclusion of external rotation [8,9]. Indeed, it is already of significant recent interest to explore the interaction of vortical patterns, as has been done in two-component settings, e.g., in [75,76] (see also references therein). Moreover, in the current setup the inclusion of three-body recombination processes as a dissipative mechanism in selective spin channels constitutes a situation that accounts for possible experimental imperfections [5]. Yet another fruitful perspective is to consider domain walls formed by two out of the three spin components with the remaining one being a nonlinear excitation of a different flavor, e.g., a vortex [77]. This setting will enable one to devise particular spin-mixing channels and consequently study dynamical pattern formation.

## ACKNOWLEDGMENTS

This work is funded by the Cluster of Excellence "Advanced Imaging of Matter" of the Deutsche Forschungsgemeinschaft (DFG)–EXC 2056–Project ID 390715994. S.I.M. gratefully acknowledges financial support from the NSF through a grant for ITAMP at Harvard University and in the framework of the Lenz-Ising Award of the University of Hamburg. This material is based upon work supported by the NSF under Grant No. PHY-2110030 (P.G.K.).

## APPENDIX A: ELEMENTS OF THE BDG EQUATION

In this Appendix the distinct matrix elements of the BdG Eq. (8) discussed in the main text are provided. In particular, the $2\times2$ submatrices $M_j$ with $j=1,\ldots,9$ have the form

$$M_1=\begin{bmatrix} A_{11} & A_{12} \\ -A_{12}^* & -A_{11}\end{bmatrix},\ M_2=\begin{bmatrix} A_{13} & A_{14} \\ -A_{14}^* & -A_{13}^*\end{bmatrix},$$

$$M_3=\begin{bmatrix} A_{15} & A_{16} \\ -A_{16}^* & -A_{15}^*\end{bmatrix},\ M_4=\begin{bmatrix} A_{13}^* & A_{14} \\ -A_{14}^* & -A_{13}\end{bmatrix},$$

$$M_5=\begin{bmatrix} A_{33} & A_{34} \\ -A_{34}^* & -A_{33}\end{bmatrix},\ M_6=\begin{bmatrix} A_{35}^* & A_{36} \\ -A_{36}^* & -A_{35}^*\end{bmatrix},$$

$$M_7=\begin{bmatrix} A_{15}^* & A_{16} \\ -A_{16}^* & -A_{15}\end{bmatrix},\ M_8=\begin{bmatrix} A_{35}^* & A_{36} \\ -A_{36}^* & -A_{35}\end{bmatrix},$$

$$M_9=\begin{bmatrix} A_{55} & A_{56} \\ -A_{56}^* & -A_{55}\end{bmatrix}. \tag{A1}$$

The corresponding matrix elements $A_{ij}$ read

$$\begin{aligned}
A_{11} &= \mathcal{H}-\mu_0+c_0\left(\left|\Psi_1^0\right|^2+2\left|\Psi_0^0\right|^2+\left|\Psi_{-1}^0\right|^2\right)\\
&\quad+c_1\left(\left|\Psi_1^0\right|^2+\left|\Psi_{-1}^0\right|^2\right),\\
A_{33} &= \mathcal{H}-\mu_1+q+c_0\left(2\left|\Psi_1^0\right|^2+\left|\Psi_0^0\right|^2+\left|\Psi_{-1}^0\right|^2\right)\\
&\quad+c_1\left(2\left|\Psi_1^0\right|^2+\left|\Psi_0^0\right|^2-\left|\Psi_{-1}^0\right|^2\right),\\
A_{55} &= \mathcal{H}-\mu_{-1}+q+c_0\left(\left|\Psi_1^0\right|^2+\left|\Psi_0^0\right|^2+2\left|\Psi_{-1}^0\right|^2\right)\\
&\quad+c_1\left(2\left|\Psi_{-1}^0\right|^2+\left|\Psi_0^0\right|^2-\left|\Psi_1^0\right|^2\right),\\
A_{12} &= c_0\Psi_0^{0^2}+2c_1\Psi_{-1}^0\Psi_1^0,\\
A_{13} &= (c_0+c_1)\Psi_1^{0^*}\Psi_0^0+2c_1\Psi_0^{0^*}\Psi_{-1}^0,\\
A_{14} &= (c_0+c_1)\Psi_1^0\Psi_0^0,\\
A_{15} &= (c_0+c_1)\Psi_{-1}^{0^*}\Psi_0^0+2c_1\Psi_0^{0^*}\Psi_1^0,\\
A_{16} &= (c_0+c_1)\Psi_{-1}^0\Psi_0^0, A_{34}=(c_0+c_1)\Psi_1^{0^2},\\
A_{35} &= (c_0-c_1)\Psi_{-1}^{0^*}\Psi_1^0, A_{36}=(c_0-c_1)\Psi_{-1}^0\Psi_1^0+c_1\Psi_0^{0^2},\\
A_{56} &= (c_0+c_1)\Psi_{-1}^{0^2}.
\end{aligned} \tag{A2}$$

Recall that $\Psi_{m_F}^0(x,y)$ denotes the relevant equilibrium solution for each magnetic phase. Substituting Eqs. (A1) and (A2) in the eigenvalue problem of Eq. (8) leads, upon numerical evaluation, to the BdG spectra given in the main text.

## APPENDIX B: IMPACT OF LARGER SYSTEM SIZES AND HIGHER-CHARGE VORTICITY

Here, we aim to generalize our findings presented in the main text by considering different system sizes and vortex charges. In particular, in the former case we systematically vary the total number of particles within the range $N\in[1\times10^3, 2\times10^4]$ while in the latter situation vortices of $S=2,3$ are explored. Experimentally higher-charge vortices can be realized using the topological phase-imprinting technique [78]. Remarkably enough, monitoring the polarization of the FM spinor system under $(q,N)$ variations reveals that it remains insensitive under such parametric changes independently of the stationary configuration (not shown for brevity). Sizable deviations are only present when higher charge vortices are contained either in a VBV or a BVB equilibrium solution. Indeed, as presented in Figs. 9(a) and 9(b), $P$ experiences drastic changes under a $(q,S)$ variation. Particularly, while $S$ increases an overall shift of $P$ towards more positive (negative) $q$ values is observed for BVB (VBV) solutions altering in this way the distinct magnetic phase transition boundaries. Since $S=2$ and 3 vortices are structures having significantly wider cores [see Figs. 9(c1)–9(c3) and 9(d1)–9(d3), respectively], when compared to the $S=1$ configurations (see the insets in Fig. 4), the above-mentioned shift can be explained as follows. Initially, we should recall that bright solitons can only be sustained in repulsive environments, via their effective trapping by nonlinear excitations such as the vortices studied herein [68]. Thus, higher charge vortices can effectively trap in a more efficient manner the bright soliton component, leading in turn to persistent over wider parametric intervals 3C entities.

Even though it is known that multiply quantized vortices are prone to decay into singly quantized vortex pairs in scalar [61,78–81] and two-component BECs [82], the fate of such higher charge entities in spinorial BEC systems remains still elusive [35]. As such, below we further investigate the stability properties of these configurations. Specifically, we focus on the simplest case scenario, namely, the one involving spinors in which the vortices have charge $S=2$. Our stability analysis reveals that doubly quantized FM VBVs and BVBs are, in principle, linearly stable configurations for values of $q\in[-4.0,-0.5)$ and $[0.2,4.0]$, respectively, that we have checked and for the particular particle number chosen. Narrow windows where oscillatory instabilities are identified, giving rise to a finite imaginary contribution of the order of $\mathrm{Im}(\Omega)\approx10^{-3}$–$10^{-2}$, occur for the VBV configuration, e.g., for $q\in[-0.75,0.65]$ and $q=-0.9$. Remarkably, seven negative-energy modes, $\mathrm{AM}_i$ $(i=1,2,\ldots,7)$, are found in the BdG spectrum of this structure as can be seen for instance in Fig. 10(a1) for $q=-1.0$.

Among these modes the lowest-lying one, $\mathrm{AM}_1$, resides close to the zero frequency axis, as in the FM $S=1$ scenario. In order to visualize the effect that the perturbation has on the VBV excitation, we invoke, as in the main text, the density difference, $\Delta\Psi_{m_F}(x,y)\equiv|\tilde{\Psi}_{m_F}(x,y)|^2-|\Psi_{m_F}(x,y)|^2$. It turns out that contrary to the $S=1$ case here $\Delta\Psi_{\pm1}(x,y)$ develops an eight-lobe dumbbell-shaped structure centered around the origin of the $(x$-$y)$ plane $(x=y=0)$ and being reminiscent of a $5g_{z^3x}$ orbital. This density difference is further found to acquire its maximum or minimum value in an alternating fashion among the distinct lobes. Importantly though, also for higher charges, the number of negative Krein modes is greater than the one anticipated for an $S=2$ VBV solution. Indeed, it is known [82] that since the two vortices are doubly quantized in this case one can assign two anomalous mode pairs to each of the two participating vortices. These yield in turn four anomalous mode pairs for such a state rather than the seven identified herein.

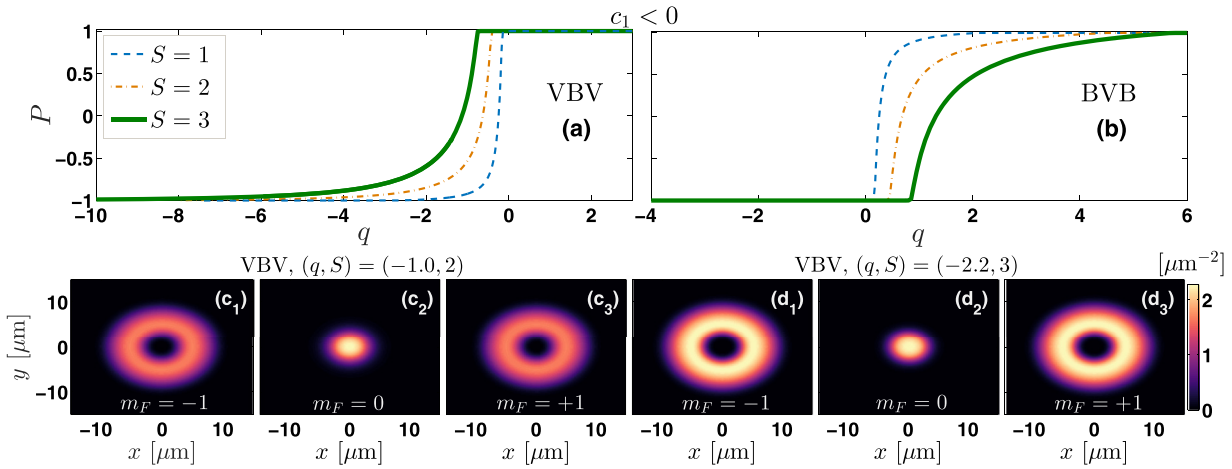


FIG. 9. Polarization, $P$, in terms of the QZ coefficient $q$ for (a) a VBV and (b) a BVB configuration upon also varying the vortex charge $S$ (see legend). An increasing $S$ prolongs the region of existence of the 3C state with respect to $q$. Note that QZ is provided in units of $\hbar\omega$. (c1–c3) [(d1–d3)] Density contours of a stationary VBV state of charge $S = 2$ [$S = 3$] for $q = -1.0$ [$q = -2.2$], i.e., within the EA phase. The FM spin-1 BEC mixture contains $N = 10^4$ $^{87}$Rb atoms.

Thus, in what follows $\Delta\Psi_{m_F}(x, y)$ is evaluated and shown in Figs. 10(b1)–10(j1) for three out of the seven modes that VBV solutions possess. Notice that in all three cases the bright soliton of the $m_F = 0$ spin component is not altered as captured by $\Delta\Psi_0(x, y) \approx 10^{-6}$. This is in contrast to the vortices of the $m_F = \pm 1$ spin components that complement one another. Evidently, perturbing the VBV solution with the eigenvector related to $\text{AM}_4$ results in an asymmetric two-lobe $\Delta\Psi_{\pm 1}(x, y)$ configuration resembling a $2p$ orbital. The latter is oriented along the antidiagonal $x = -y$ but is slightly shifted from it counterclockwise. $\Delta\Psi_{-1}(x > 0, y) > 0$ while $\Delta\Psi_{+1}(x > 0, y) < 0$. $\text{AM}_5$ leads to a centered around the origin $4f_{xz^2}$ orbital-like configuration, namely, a six dumbbell-shaped lobe structure [Figs. 10(e1) and 10(g1). Notice that the density difference maximizes and minimizes in an alternating manner as we go from one lobe to the other. Here, dynamical activation of $\text{AM}_4$ unveils the formation of antiphase triangular patterns in the vortex $m_F = \pm 1$ components which along with an intact bright soliton $m_F = 0$ component precess around the trap center. Contrary to the above dynamics, perturbing the VBV entity with $\text{AM}_5$ leads to the formation and robust propagation of a deformed structure. The two vortices perform an irregular out-of-phase precession leaving in this way the bright soliton in the $m_F = 0$ component intact, but instead of forming triangles they feature dipolarly elongated density distributions being inverted between the $m_F = +1$ and $-1$ components. However, addition of the eigenvector associated with $\text{AM}_7$ entails a completely different deformation. $\Delta\Psi_{\pm 1}(x, y)$ develops a $3d_{xz}$ orbital-like pattern [Figs. 10(h1) and 10(j1)], that is, a four-lobe cloverleaf distribution with the symmetric hyperfine components complementing one another.

Dynamical activation of $\text{AM}_7$ leads to a breathing core VBV structure that performs an irregular (out-of-phase) precession having spatially anisotropic and oppositely elongated with respect to each other symmetric spin components. The remaining eigenvectors associated with $\text{AM}_2$, $\text{AM}_3$, and $\text{AM}_6$ result, respectively, in a $\Delta\Psi_{m_F}(x, y)$ that has a $4d_{xz}$ orbital structure in all three hyperfine components, having $\Delta\Psi_0(x, y) \approx 10^{-8}$ and being centered at the origin of the $(x$-$y)$ plane. $\text{AM}_3$ leads to a $2p$ orbital distribution like the one found for the $\text{AM}_4$ mode but with the two lobes being slightly shifted with respect to each other while residing antidiametrically along the diagonal $x = y$. Here, $\Delta\Psi_{-1}(x, y) = \Delta\Psi_{+1}(x, y)$ and both are complementary to the $m_F = 0$ bright soliton component. Additionally, the effect of $\text{AM}_6$ closely resembles that found for $\text{AM}_7$ but with the symmetric vortex components having now exactly the same structure while being complementary to $\Delta\Psi_0(x, y)$ which is now finite. Finally, we note that $\text{AM}_1$ and $\text{AM}_2$ perform an eigenfrequency zero crossing at $q = -0.4$ but are not responsible for an instability [$\text{Im}(\Omega = 0)$]. The rest of the AMs, i.e., $\text{AM}_i$ with $i = 3, \ldots, 7$, decrease in frequency but only around $q = -0.05$ cross the zero frequency axis signaling the termination of this nonlinear excitation.

On the other hand, $S = 2$ BVB solutions destabilize via two eigenfrequency zero crossings of the two principal AMs present in the BdG spectrum of this configuration, namely, $\text{AM}_3$ which is the higher-lying negative-energy mode and $\text{AM}_2$ being the lower-lying one. These destabilizations take place at $q = 0$, i.e., at the threshold ($q = 0$) separating the EP and the EA phases, and $q = 0.15$. However, among the two only the second destabilization produces a sizable imaginary component being of the order of $\text{Im}(\Omega) \approx 10^{-2}$. Also an oscillatory instability is identified for the $S = 2$ BVB entity appearing at around $q = 0.7$. This is an instability that owes its existence to the collision of $\text{AM}_3$ with a positive Krein mode giving rise to an eigenfrequency quartet similar to those identified for the $S = 1$ structures. There exists also a third anomalous mode for this BVB configuration, namely, $\text{AM}_1$, that stems from a change in sign of a background mode from positive to negative. This mode appears in the BdG spectrum for $q = 0.6$ and remains present as $q$ is further lowered towards the phase transition point.

The above-discussed modes are illustrated in Fig. 10(a2) while their activation leads to deformations of the stationary

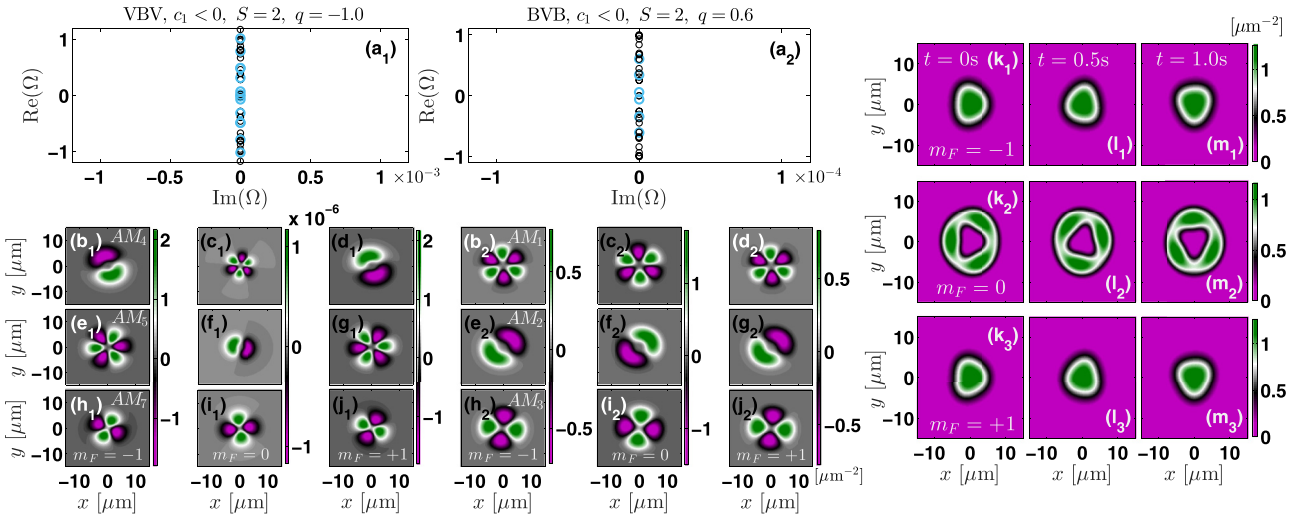


FIG. 10. (a1) [(a2)] BdG spectra of doubly quantized, $S = 2$, VBV [BVB] stationary states for $q = -1.0$ [$q = 0.6$] and for FM interactions ($c_1 < 0$). Notice the absence of imaginary eigenfrequencies for both entities that demonstrates their spectral stability. Remarkably seven AM$i$ (with $i = 1, 2, \ldots, 7$) pairs, being marked by light blue circles, are present for the VBV configuration in contrast to the three found for a BVB solution. (b1–j$_1$) [(b2–j$_2$)] 2D contour plots measuring the density difference $\Delta\Psi_{m_F}(x, y) \equiv |\tilde{\Psi}_{m_F}(x, y)|^2 - |\Psi_{m_F}(x, y)|^2$ for a VBV [BVB] solution and for $q = -1.0$ [$q = 0.6$] (see legends). (k$_1$–m$_3$) Snapshots of the density, $|\tilde{\Psi}_{m_F}(x, y)|^2$, of an $S = 2$ BVB solution for $q = 0.6$ perturbed via the eigenvector associated with AM$_1$. The distinct spin components are shown, respectively, for $t = 0$, 0.5, and 1.0 s (see legends). All densities are illustrated in dimensional units. The BdG frequencies $\Omega$ are in units of $\omega$ and $q$ is provided in terms of $\hbar\omega$.

$S = 2$ BVB state, an effect that is measured via $\Delta\Psi_{m_F}(x, y)$ shown in Figs. 10(b2)–10(j2). Notice that $\Delta\Psi_{m_F}(x, y)$ is finite irrespectively of which mode, i.e., AM$_1$, AM$_2$, or AM$_3$, is activated. Particularly, for the first mode at hand, $\Delta\Psi_{m_F}(x, y)$ acquires a $4f_{xz^2}$ orbital-like distribution as the one found for the perturbed via AM$_5$ VBV entity. Here though, $\Delta\Psi_{-1}(x, y) = \Delta\Psi_{+1}(x, y)$ while both are complementary to the $m_F = 0$ vortex component. Likewise, the density difference assumes a $2p$ orbital-like structure once AM$_2$ is taken into account, a result similar to the one found for the VBV solutions when AM$_3$ was triggered.

Finally, the eigenvector related to AM$_3$ is responsible for a $3d_{xz}$ deformation imprinted in $\Delta\Psi_{m_F}(x, y)$ like the one found for the VBV structure when perturbed with the eigenvector associated with AM$_7$ [see here Figs. 10(h2)–10(j2)]. However, here $\Delta\Psi_{-1}(x, y) = \Delta\Psi_{+1}(x, y)$ while both are complementary to $\Delta\Psi_0(x, y)$ that is also finite in this case.

A case example showcasing the dynamical evolution of a perturbed $S = 2$ configuration is provided in Figs. 10(k1)–10(m3) for $q = 0.6$. Notice the structural deformation of the ensuing BVB structure caused by the addition of the eigenvector related to AM$_1$. Evidently, already at $t = 0$ s a triangular pattern [54,57,58], breaking the radial symmetry of the trap along the azimuthal direction, is seen in Figs. 10(k1)–10(k3), the precessional motion of which is then followed for times up to $t = 1.0$ s [Figs. 10(m1)–10(m3)], an outcome verifying that, indeed, this deformation is caused by the above-identified azimuthal mode with triangular symmetry (i.e., an $e^{3i\theta}$ perturbation mode). It is also worthwhile to mention that similar findings are also present for AF spinor BECs (not shown).


[1] D. M. Stamper-Kurn, M. R. Andrews, A. P. Chikkatur, S. Inouye, H.-J. Miesner, J. Stenger, and W. Ketterle, Phys. Rev. Lett. **80**, 2027 (1998).

[2] J. Stenger, S. Inouye, D. M. Stamper-Kurn, H.-J. Miesner, A. P. Chikkatur, and W. Ketterle, Nature (London) **396**, 345 (1998).

[3] M.-S. Chang, Q. Qin, W. Zhang, L. You, and M. S. Chapman, Nat. Phys. **1**, 111 (2005).

[4] A. Widera, F. Gerbier, S. Fölling, T. Gericke, O. Mandel, and I. Bloch, New J. Phys. **8**, 152 (2006).

[5] S. J. Huh, K. Kim, K. Kwon, and J.-Y. Choi, Phys. Rev. Res. **2**, 033471 (2020).

[6] Y. Kawaguchi and M. Ueda, Phys. Rep. **520**, 253 (2012).

[7] D. M. Stamper-Kurn and M. Ueda, Rev. Mod. Phys. **85**, 1191 (2013).

[8] C. J. Pethick and H. Smith, *Bose-Einstein Condensation in Dilute Gases* (Cambridge University Press, Cambridge, England, 2002).

[9] L. Pitaevskii and S. Stringari, *Bose-Einstein Condensation* (Oxford University Press, New York, 2003).

[10] P. Kevrekidis, D. Frantzeskakis, and R. Carretero-González, *The Defocusing Nonlinear Schrödinger Equation* (SIAM, Philadelphia, PA, 2015).

[11] K. Kim, J. Hur, S. J. Huh, S. Choi, and J.-Y. Choi, Phys. Rev. Lett. **127**, 043401 (2021).

[12] C.-M. Schmied, T. Gasenzer, M. K. Oberthaler, and P. G. Kevrekidis, Commun. Nonlinear Sci. Numer. Simulat. **83**, 105050 (2020).

[13] K. M. Mittal, S. I. Mistakidis, P. G. Kevrekidis, and P. Schmelcher, Phys. Rev. A **102**, 013302 (2020).

[14] L. Li, Z. Li, B. A. Malomed, D. Mihalache, and W. M. Liu, Phys. Rev. A **72**, 033611 (2005).

[15] W. Zhang, Ö. E. Müstecaplıoğlu, and L. You, Phys. Rev. A **75**, 043601 (2007).

[16] H. E. Nistazakis, D. J. Frantzeskakis, P. G. Kevrekidis, B. A. Malomed, and R. Carretero-González, Phys. Rev. A **77**, 033612 (2008).

[17] P. Szankowski, M. Trippenbach, and E. Infeld, Eur. Phys. J. D **65**, 49 (2011).

[18] A. Romero-Ros, G. C. Katsimiga, P. G. Kevrekidis, and P. Schmelcher, Phys. Rev. A **100**, 013626 (2019).

[19] X. Chai, D. Lao, K. Fujimoto, R. Hamazaki, M. Ueda, and C. Raman, Phys. Rev. Lett. **125**, 030402 (2020).

[20] X. Chai, D. Lao, K. Fujimoto, and C. Raman, Phys. Rev. Res. **3**, L012003 (2021).

[21] C.-M. Schmied and P. G. Kevrekidis, Phys. Rev. A **102**, 053323 (2020).

[22] T. M. Bersano, V. Gokhroo, M. A. Khamehchi, J. D'Ambroise, D. J. Frantzeskakis, P. Engels, and P. G. Kevrekidis, Phys. Rev. Lett. **120**, 063202 (2018).

[23] G. C. Katsimiga, S. I. Mistakidis, P. Schmelcher, and P. G. Kevrekidis, New J. Phys. **23**, 013015 (2021).

[24] S. Lannig, C.-M. Schmied, M. Prüfer, P. Kunkel, R. Strohmaier, H. Strobel, T. Gasenzer, P. G. Kevrekidis, and M. K. Oberthaler, Phys. Rev. Lett. **125**, 170401 (2020).

[25] K. Fujimoto, R. Hamazaki, and M. Ueda, Phys. Rev. Lett. **122**, 173001 (2019).

[26] H.-J. Miesner, D. M. Stamper-Kurn, J. Stenger, S. Inouye, A. P. Chikkatur, and W. Ketterle, Phys. Rev. Lett. **82**, 2228 (1999).

[27] T. Świsłocki and M. Matuszewski, Phys. Rev. A **85**, 023601 (2012).

[28] H. T. C. Stoof, E. Vliegen, and U. Al Khawaja, Phys. Rev. Lett. **87**, 120407 (2001).

[29] J.-P. Martikainen, A. Collin, and K.-A. Suominen, Phys. Rev. Lett. **88**, 090404 (2002).

[30] T. Ollikainen, K. Tiurev, A. Blinova, W. Lee, D. S. Hall, and M. Möttönen, Phys. Rev. X **7**, 021023 (2017).

[31] D. S. Hall, M. W. Ray, K. Tiurev, E. Ruokokoski, A. H. Gheorghe, and M. Möttönen, Nat. Phys. **12**, 478 (2016).

[32] W. Lee, A. H. Gheorghe, K. Tiurev, T. Ollikainen, M. Möttönen, and D. S. Hall, Sci. Adv. **4**, eaao3820 (2018).

[33] K.-P. Marzlin, W. Zhang, and B. C. Sanders, Phys. Rev. A **62**, 013602 (2000).

[34] T. Mizushima, K. Machida, and T. Kita, Phys. Rev. Lett. **89**, 030401 (2002).

[35] A. E. Leanhardt, Y.-I. Shin, D. Kielpinski, D. E. Pritchard, and W. Ketterle, Phys. Rev. Lett. **90**, 140403 (2003).

[36] J. W. Reijnders, F. J. M. Van Lankvelt, K. Schoutens, and N. Read, Phys. Rev. A **69**, 023612 (2004).

[37] J.-Y. Choi, W. J. Kwon, and Y.-I. Shin, Phys. Rev. Lett. **108**, 035301 (2012).

[38] S.-W. Song, L. Wen, C.-F. Liu, S.-C. Gou, and W.-M. Liu, Front. Phys. **8**, 302 (2013).

[39] T. Mizushima, K. Machida, and T. Kita, Phys. Rev. A **66**, 053610 (2002).

[40] U. Leonhardt and G. E. Volovik, JETP Lett. **72**, 46 (2000).

[41] J. Ruostekoski and J. R. Anglin, Phys. Rev. Lett. **91**, 190402 (2003).

[42] J. Lovegrove, M. O. Borgh, and J. Ruostekoski, Phys. Rev. A **86**, 013613 (2012).

[43] S. W. Seo, S. Kang, W. J. Kwon, and Y.-I. Shin, Phys. Rev. Lett. **115**, 015301 (2015).

[44] Y. Xiao, M. O. Borgh, L. S. Weiss, A. A. Blinova, J. Ruostekoski, and D. S. Hall, Commun. Phys. **4**, 1 (2021).

[45] L. Sadler, J. Higbie, S. Leslie, M. Vengalattore, and D. Stamper-Kurn, Nature (London) **443**, 312 (2006).

[46] L. S. Weiss, M. O. Borgh, A. Blinova, T. Ollikainen, M. Möttönen, J. Ruostekoski, and D. S. Hall, Nat. Commun. **10**, 1 (2019).

[47] H. Takeuchi, Phys. Rev. A **104**, 013316 (2021).

[48] H. Takeuchi, Phys. Rev. Lett. **126**, 195302 (2021).

[49] A. P. C. Underwood, D. Baillie, P. B. Blakie, and H. Takeuchi, Phys. Rev. A **102**, 023326 (2020).

[50] J. Lovegrove, M. O. Borgh, and J. Ruostekoski, Phys. Rev. A **93**, 033633 (2016).

[51] D. V. Skryabin, Phys. Rev. A **63**, 013602 (2000).

[52] P. Kevrekidis and D. Frantzeskakis, Rev. Phys. **1**, 140 (2016).

[53] I-K. Liu, S.-C. Gou, and H. Takeuchi, Phys. Rev. Res. **2**, 033506 (2020).

[54] R. Saint-Jalm, P. C. M. Castilho, É. Le Cerf, B. Bakkali-Hassani, J.-L. Ville, S. Nascimbene, J. Beugnon, and J. Dalibard, Phys. Rev. X **9**, 021035 (2019).

[55] S. K. Adhikari, Phys. Rev. E **104**, 024207 (2021).

[56] G. C. Katsimiga, S. I. Mistakidis, T. M. Bersano, M. K. H. Ome, S. M. Mossman, K. Mukherjee, P. Schmelcher, P. Engels, and P. G. Kevrekidis, Phys. Rev. A **102**, 023301 (2020).

[57] K. Kwon, K. Mukherjee, S. J. Huh, K. Kim, S. I. Mistakidis, D. K. Maity, P. G. Kevrekidis, S. Majumder, P. Schmelcher, and J.-Y. Choi, Phys. Rev. Lett. **127**, 113001 (2021).

[58] D. K. Maity, K. Mukherjee, S. I. Mistakidis, S. Das, P. G. Kevrekidis, S. Majumder, and P. Schmelcher, Phys. Rev. A **102**, 033320 (2020).

[59] A. Vinit and C. Raman, Phys. Rev. A **95**, 011603(R) (2017).

[60] S. Kang, S. W. Seo, J. H. Kim, and Y.-I. Shin, Phys. Rev. A **95**, 053638 (2017).

[61] H. Pu, C. K. Law, J. H. Eberly, and N. P. Bigelow, Phys. Rev. A **59**, 1533 (1999).

[62] N. N. Klausen, J. L. Bohn, and C. H. Greene, Phys. Rev. A **64**, 053602 (2001).

[63] Notice that in such a setting phenomena associated with multiple orbital occupation and signatures of fragmentation should be expected to be absent; for a relevant discussion, see, e.g., [13].

[64] L. Santos, M. Fattori, J. Stuhler, and T. Pfau, Phys. Rev. A **75**, 053606 (2007).

[65] S. R. Leslie, J. Guzman, M. Vengalattore, J. D. Sau, M. L. Cohen, and D. M. Stamper-Kurn, Phys. Rev. A **79**, 043631 (2009).

[66] E. M. Bookjans, A. Vinit, and C. Raman, Phys. Rev. Lett. **107**, 195306 (2011).

[67] K. J. H. Law, P. G. Kevrekidis, and L. S. Tuckerman, Phys. Rev. Lett. **105**, 160405 (2010).

[68] M. Pola, J. Stockhofe, P. Schmelcher, and P. G. Kevrekidis, Phys. Rev. A **86**, 053601 (2012).

[69] K. Mukherjee, S. I. Mistakidis, P. G. Kevrekidis, and P. Schmelcher, J. Phys. B: At. Mol. Opt. Phys. **53**, 235002 (2020).

[70] C. T. Kelley, *Solving Nonlinear Equations with Newton's Method* (SIAM, Philadelphia, PA, 2003).

[71] H. Kiehn, S. I. Mistakidis, G. C. Katsimiga, and P. Schmelcher, Phys. Rev. A **100**, 023613 (2019).

[72] N. P. Proukakis and B. Jackson, J. Phys. B: At. Mol. Opt. Phys. **41**, 203002 (2008).

[73] V. Achilleos, D. Yan, P. G. Kevrekidis, and D. J. Frantzeskakis, New J. Phys. **14**, 055006 (2012).

[74] D. Yan, R. Carretero-González, D. J. Frantzeskakis, P. G. Kevrekidis, N. P. Proukakis, and D. Spirn, Phys. Rev. A **89**, 043613 (2014).

[75] A. Richaud, V. Penna, R. Mayol, and M. Guilleumas, Phys. Rev. A **101**, 013630 (2020).

[76] A. Richaud, V. Penna, and A. L. Fetter, Phys. Rev. A **103**, 023311 (2021).

[77] X. Yu and P. B. Blakie, Phys. Rev. Res. **3**, 023043 (2021).

[78] A. E. Leanhardt, A. Görlitz, A. P. Chikkatur, D. Kielpinski, Y.-I. Shin, D. E. Pritchard, and W. Ketterle, Phys. Rev. Lett. **89**, 190403 (2002).

[79] M. Möttönen, T. Mizushima, T. Isoshima, M. M. Salomaa, and K. Machida, Phys. Rev. A **68**, 023611 (2003).

[80] Y.-i. Shin, M. Saba, M. Vengalattore, T. A. Pasquini, C. Sanner, A. E. Leanhardt, M. Prentiss, D. E. Pritchard, and W. Ketterle, Phys. Rev. Lett. **93**, 160406 (2004).

[81] J. A. M. Huhtamäki, M. Möttönen, T. Isoshima, V. Pietilä, and S. M. M. Virtanen, Phys. Rev. Lett. **97**, 110406 (2006).

[82] P. G. Kevrekidis, D. J. Frantzeskakis, and R. Carretero-González, *The Defocusing Nonlinear Schrödinger Equation: From Dark Solitons to Vortices and Vortex Rings* (SIAM, Philadelphia, PA, 2015).